Turbulent three-dimensional dielectric electrohydrodynamic convection between two plates

A. Kourmatzis[1] and J. S. Shrimpton[2]†

[1] Clean Combustion Group, Aerospace, Mechanical and Mechatronic Engineering, University of Sydney, Sydney, NSW 2006, Australia

[2] Energy Technology Research Group, School of Engineering Sciences, University of Southampton, Southampton SO17 1BJ, UK

The fundamental mechanisms responsible for the creation of electrohydrodynamically driven roll structures in free electroconvection between two plates are analysed with reference to traditional Rayleigh–Bénard convection (RBC). Previously available knowledge limited to two dimensions is extended to three-dimensions, and a wide range of electric Reynolds numbers is analysed, extending into a fully inherently three-dimensional turbulent regime. Results reveal that structures appearing in three-dimensional electrohydrodynamics (EHD) are similar to those observed for RBC, and while two-dimensional EHD results bear some similarities with the three-dimensional results there are distinct differences. Analysis of two-point correlations and integral length scales show that full three-dimensional electroconvection is more chaotic than in two dimensions and this is also noted by qualitatively observing the roll structures that arise for both low ($Re_E = 1$) and high electric Reynolds numbers (up to $Re_E = 120$). Furthermore, calculations of mean profiles and second-order moments along with energy budgets and spectra have examined the validity of neglecting the fluctuating electric field E_i' in the Reynolds-averaged EHD equations and provide insight into the generation and transport mechanisms of turbulent EHD. Spectral and spatial data clearly indicate how fluctuating energy is transferred from electrical to hydrodynamic forms, on moving through the domain away from the charging electrode. It is shown that E_i' is not negligible close to the walls and terms acting as sources and sinks in the turbulent kinetic energy, turbulent scalar flux and turbulent scalar variance equations are examined. Profiles of hydrodynamic terms in the budgets resemble those in the literature for RBC; however there are terms specific to EHD that are significant, indicating that the transfer of energy in EHD is also attributed to further electrodynamic terms and a strong coupling exists between the charge flux and variance, due to the ionic drift term.

Key words: buoyancy-driven instability, dielectrics, electrohydrodynamic effects

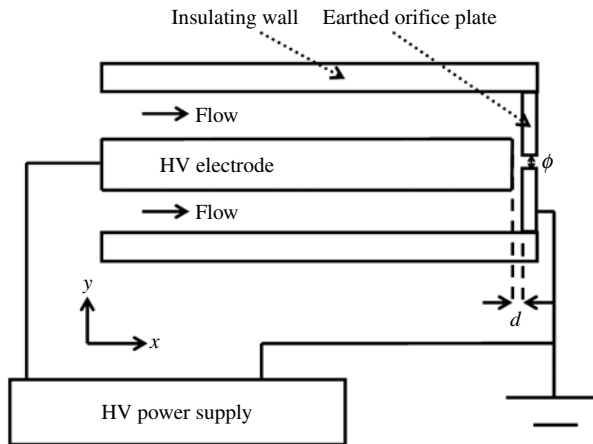† Email address for correspondence: john.shrimpton@gmail.com

FIGURE 1. Schematic of charge injection atomizer operation.

1. Introduction

Electrohydrodynamics (EHD) is the interdisciplinary field dealing with the interaction between hydrodynamic and electrical forces (Castellanos 1998). The area has a number of industrial applications that range from electrostatic spraying (Kim & Turnbull 1976; Kelly 1984; Bailey 1986; Bankston *et al.* 1988; Lehr & Hiller 1993; Balachandran *et al.* 1999; Ye, Domnick & Pulli 2005) to electrostatic precipitators (Davidson & McKinney 1989, 1991; Yamamoto *et al.* 2006). Here, discussion is restricted to pure isothermal dielectric liquids, where charged dipoles and monopoles are separated by neutral entities (Crowley 1999) and electric charge may reside for relatively long periods in the liquid volume.

In practical spraying applications, such as in charge injection atomization (Kelly 1984, 1990; Shrimpton & Yule 2003; Rigit & Shrimpton 2006), fine sprays are achieved via injecting charge into a dielectric liquid through a charge-emitting electrode that is commonly held at negative high voltage ranging from 2–10 kV. Within the device, the high-voltage (HV) electrode to orifice plane gap is typically of length d and comparable to the orifice diameter, ϕ, as shown in figure 1. Between the HV electrode and grounded orifice plate, the area referred to as the inter-electrode gap of length d, the high electric fields and significant charge density result in EHD chaos developing (Shrimpton & Kourmatzis 2010). Unfortunately such devices have been designed and are operated without the support of a good physical understanding of the electrohydrodynamics in this region. A motivation for this study is to understand the EHD in this electrode gap region and to use this knowledge to improve the performance of charge injection atomizers.

A more common example of a charge-laden dielectric fluid is air in electrostatic precipitators (ESP), where corona-laden air and imposed electric fields charge unwanted particles and remove them from a dusty gas flow (Davidson & McKinney 1989, 1991; Yamamoto *et al.* 2006). Although the governing equations pertaining to flow of electrically charged air, such as in an ESP, are the same as for systems containing dielectric liquids there are distinct differences. An electrically charged fluid element has two velocity components U_i and κE_i where U_i is the bulk flow velocity and κE_i is the ionic drift velocity component. For negatively charged carriers in air, the ionic mobility, $\kappa \sim 1 \times 10^{-6}$ (m^2 (Vs)$^{-1}$), is approximately three orders of

magnitude greater than that of a dielectric liquid, such as a hydrocarbon fuel. This results in a different coupling between the bulk flow of the air and the flow attributed to electrical force, meaning that in ESPs $\kappa E_i \gg U_i$ due to the high mobility which results in a one-way coupling between the flow field and the electrical forces. In such systems the flow field is driven by κE_i but the electric field is not strongly influenced by the flow field (Soldati & Banerjee 1998). The study by Soldati & Banerjee (1998) examined the energy budget contribution by the production and transport terms in the turbulent kinetic energy equation for the EHD case. The domain studied was a plane–plane system with an imposed cross-flow. Other investigations on EHD turbulence and instability pertaining to ESPs have been undertaken by Yamamoto *et al.* (2006) and Hong, Wang & Wu (2008); however as they were also one-way coupled studies they are not commented on further here. With the dielectric liquids investigated in this paper, such as insulating hydrocarbon fuels, the mobility may be as low as 10^{-10} m^2 (Vs)$^{-1}$ (Melcher 1981) leading to $\kappa E_i \sim U_i$. The coupling can result in chaotic roll structures appearing, similar to the thermal Rayleigh–Bénard-convection (RBC) case, and the literature pertaining to this area is now reviewed.

The investigation of roll structures in thermal RBC is well-documented (Getling 1998; Worner & Grotzbach 1998; Chandra & Grotzbach 2008). Here, three-dimensional roll structures are produced by the input of thermal energy as opposed to electrical energy and several studies have drawn analogies between the two areas of physics (Tobazeon 1984; Castellanos 1991; Atten 1996, 1998; Vazquez, Perez & Castellanos 1996). In the EHD case, it is mainly the Lorentz body force term (Castellanos 1991, 1998) ρQE_i in the Navier–Stokes (NS) equations that drives instabilities while in the thermal case it is a thermal source term $\rho(1 + \alpha(\Phi - \Phi_0))g_i$ arising from the Boussinesq approximation, with α being the coefficient of thermal expansion, ρ being the density, Q being the space change and Φ_0 a reference temperature (Getling 1998; Shishkina & Wagner 2006; Verzicco & Sreenivasan 2008). Therefore, in the thermal case, the gravitational potential energy gradient is an important driving parameter, and is constant in both space and time. In the EHD case there is a highly nonlinear coupling between charge distribution and electric field in the space charge transport equation. Hence, the electrical potential energy gradient is now no longer a constant in either space or time. Thermal RBC is well-understood and extensive research exists which is aimed towards the better understanding of both ordered convective motion as well as more turbulent convective motion (Xi & Gunton 1993; Worner & Grotzbach 1998; Chavanne *et al.* 2001; Shishkina & Wagner 2006; Chandra & Grotzbach 2008; Verzicco & Sreenivasan 2008). The analogous dielectric EHD however has not been as well-examined, and in this paper analysis of turbulent dielectric EHD in three dimensions is presented for the first time. RBC will be refered to in order to draw similarities between the two cases.

As in RBC, the analogous electrical studies have involved theoretical analyses such as those carried out by Atten (1996), Schneider & Watson (1970), Hopfinger & Gosse (1971) and Castellanos (1991, 1998) which have concentrated on understanding the onset of instability as well as how the electrical forces couple to the hydrodynamic forces. More precise analysis via two-dimensional numerical investigations, such as more recent studies by Chicon, Castellanos & Martin (1997) and Vazquez, Gheorgiou & Castellanos (2006, 2008) showed how the structure of rolls is affected by the injected charge, and electric field present. Strong and weak injection regimes have been identified and investigated, where this terminology refers to the 'strength' of charge injection, directly related to the value of charge density at the injecting electrode (Vazquez *et al.* 2006, 2008), and these regimes may be more

thoroughly classified through non-dimensional governing equations, which shall be subsequently presented.

Computational studies of EHD free convection have been restricted to two dimensions. Given the nonlinearity of the EHD problem researchers have turned to 'special' numerical treatment where Chicon *et al.* (1997) have used a particle injection scheme, and Vazquez *et al.* (2006, 2008) have used both particle injection schemes and a finite-element–flux-corrected-transport (FE-FCT) method that employs both a low-order and high-order scheme where the low-order scheme includes diffusion so has to avoid solution instability, and the higher-order scheme is utilized in order to provide a more accurate solution (Vazquez *et al.* 2008). More recently, Perez *et al.* (2009) and Traore *et al.* (2010) have used a total variation diminishing (TVD) finite-volume scheme that includes artificial diffusion near the boundary and is nominally second-order. While these numerical methods are suitable for a wide range of EHD parameters, these authors have shown that a conventional globally second-order finite volume scheme can be used to simulate EHD flow quite accurately, so long as the limitations are clearly defined. More details on the implementation of a finite volume scheme to EHD shall be presented in a separate publication.

Previous authors have determined that the variation of charge and roll velocity amplitude is unstable with time (Vazquez *et al.* 2008) when in the nonlinear regime, and the level of instability directly depends on the governing non-dimensional numbers of the problem, e.g. strong injection simulations with higher Rayleigh numbers yield a greater fluctuation of space charge and velocity amplitude (Vazquez *et al.* 2008). In this paper, this knowledge is extended by examining three-dimensional roll structures, both qualitatively and quantitatively, for a very similar geometry as that used by Vazquez *et al.* (2008) using similar non-dimensional quantities. The reader should also note that most of the investigations described above concentrate on analysing instability criteria and electroconvection via deterministically investigating electroconvective roll structures. There is little work on EHD turbulence where a length scale distribution exists, and this is a focal point of this paper.

One of the very few theoretical papers published on two-way coupled EHD turbulence is that of Hopfinger & Gosse (1971). They claim that the averaged EHD equations may be simplified by a simple order-of-magnitude analysis. Their approach immediately deems any term containing E_i' negligible, greatly simplifying the EHD Reynolds-averaged Navier–Stokes (RANS) equations which are presented in Kourmatzis & Shrimpton (2009). The assumption of Hopfinger & Gosse (1971) is a scaling analysis for the simple one-dimensional electroconvective problem between two plates, where the overbar indicates a time average:

$$\frac{\partial \overline{E_1}}{\partial x_1} \sim \frac{\overline{E_1}}{l_0} \tag{1.1}$$

and

$$\frac{\partial \overline{E_1'}}{\partial x_1} \sim \frac{\overline{E_1'}}{l} \tag{1.2}$$

where l is a length scale of turbulence and l_0 is a large-scale reference length. Utilizing Gauss's law:

$$\frac{\overline{E_1'}}{\overline{E_1}} \sim \frac{l}{l_0} \frac{q'}{\overline{Q}}. \tag{1.3}$$

Hopfinger & Gosse then note that since $q' \ll \overline{Q}$, if the turbulent length scale is small then $E'_i/\overline{E_i} \ll 1$ where q' is the fluctuating value of charge. Assuming their approximation is valid then the modelling of EHD turbulence becomes a much simpler problem; however this assumption has not, until now, been analysed.

1.1. *Plan and scope*

The scope of the paper is two-fold. The first aim is to revisit the problem of electroconvection between two plates qualitatively and deterministically in real and spectral space in order to make comments regarding new features of EHD flow acquired as a result of three-dimensional simulations. The focus is on the distribution of length scales and thus the promotion of turbulent mixing that occurs due to the presence of a third dimension in combination with elevated electrical Reynolds number. The paper does not examine instability thresholds or perturbation growth, which are concepts that have been well-classified in the literature (Castellanos 1991, 1998). However, it should be noted that the method used in this paper does reproduce instability regimes and hysteresis behaviour shown elsewhere (Chicon *et al.* 1997; Vazquez *et al.* 2006, 2008) for the strong injection regimes considered here, where a future publication shall address numerical implementation in much greater detail. A further aspect of the first main aim is to analyse the transfer of energy from electrical to hydrodynamic terms in spectral space but also to gain an understanding of how energy is distributed amongst the eddy length scales or wavenumbers in real and spectral space. These features shall be analysed as a function of non-dimensional numbers, the latter being explained in § 2.

The second aim is to re-visit the assumption by Hopfinger & Gosse (1971), to test its validity and therefore to examine second-order moment terms and budgets with the overall aim of understanding EHD turbulence under strong injection from a statistical point of view. A final minor aim is to make a comment on the practical significance of the work here by making reference to the internal EHD flow of a charge injection atomizer.

The paper is organized as follows: firstly, the governing equations of EHD are stated and the significance of the relevant non-dimensional numbers discussed. Alongside these, the governing equations for RBC while employing a Boussinesq approximation are also presented, and this is done in order to draw analogies between the two cases. The geometry used shall then be presented, along with the boundary conditions employed and the choice of spatial and temporal discretization. A short section regarding validation of the method shall then be provided followed by the results, which shall include a qualitative discussion of the roll structures appearing and how they compare to previous two-dimensional simulations. Quantitative analysis shall concentrate on bivariate distributions and two-dimensional and one-dimensional two-point correlations in space. This is then followed by the presentation of compensated energy and dissipation spectra which further explain how turbulent kinetic and electrical energies are distributed amongst length scales. Examination of profiles of mean and second-order moments is then conducted and these profiles are utilized in order to investigate the assumptions of Hopfinger & Gosse (1971) and to gain a better understanding of EHD turbulence.

2. Problem formulation

2.1. *Physics and governing equations*

Charge transport may be due to diffusion, convection, and ionic drift due to an electric field gradient, whereas heat may be transported by convection and diffusion

(conduction) alone, where viscous dissipation, along with the Dp/Dt term and Joule heating are ignored (Getling 1998; Shishkina & Wagner 2006; Verzicco & Sreenivasan 2008). It is useful to present the governing equations in their non-dimensional form, and firstly, relevant scales are presented (Kourmatzis & Shrimpton 2009):

$$V^* = V/V_0, \quad E^* = V_0/d_0, \quad U^* = U/U_0, \quad Q^* = Q/Q_{ref}, \\ t^* = t/(d_0/U_0), \quad \Phi^* = \Phi/\Phi_0. \tag{2.1}$$

Throughout the paper, V is the voltage (volts), E is the electric field (V m^{-1}), U is the fluid velocity (m s^{-1}), Q is the space charge (C kg^{-1}), t is the time (s), D_V is the permittivity (F m^{-1}), C_P the specific heat (J kg^{-1} K^{-1}), k the thermal conductivity (W m^{-1} K^{-1}), α the thermal expansion coefficient (K^{-1}) and for forced convection $Q_{ref} = D_V V_0/\rho_0 d_0^2$. Using this scaling the non-dimensional governing equations for EHD for a unipolar charge species in a pure incompressible forced flow (Kourmatzis & Shrimpton 2009) and for the RBC case are

$$\frac{\partial}{\partial x_i^*}(U_i^*) = 0 \tag{2.2}$$

$$\frac{\partial}{\partial t^*}(U_i^*) + \frac{\partial}{\partial x_j^*}(U_i^* U_j^*) = \frac{1}{Re}\frac{\partial}{\partial x_j^*}\left(\frac{\partial U_i^*}{\partial x_j^*}\right) - \frac{\partial p^*}{\partial x_i^*} + \underbrace{\frac{Gr_E}{Re^2}Q^* E_i^*}_{EHD} + \underbrace{\frac{Gr}{Re^2}g_i^*(\Phi^* - 1)}_{RBC} \tag{2.3}$$

$$\frac{\partial}{\partial t^*}(Q^*) + \frac{\partial}{\partial x_i^*}(U_i^* Q^*) = \frac{1}{Re}\frac{1}{Sc_E}\frac{\partial}{\partial x_i^*}\left(\frac{\partial Q^*}{\partial x_i^*}\right) - \frac{\kappa_0 E_0}{U_0}\left(E_i^*\frac{\partial Q^*}{\partial x_i^*} + Q^{*2}\right) \tag{2.4}$$

$$\frac{\partial}{\partial t^*}(\Phi^*) + \frac{\partial}{\partial x_i^*}(\Phi^* U_i^*) = \frac{1}{Re}\frac{1}{Pr}\frac{\partial}{\partial x_i^*}\left(\frac{\partial \Phi^*}{\partial x_i^*}\right) \tag{2.5}$$

$$\frac{\partial}{\partial x_i^*}\left(\frac{\partial V^*}{\partial x_i^*}\right) = -Q^* \tag{2.6}$$

where

$$Gr_E = \frac{\rho_0^2 V_0 d_0^2}{\mu_0^2}Q_{ref} \tag{2.7}$$

$$Re = \frac{\rho_0 U_0 d_0}{\mu_0} \tag{2.8}$$

$$Sc_E = \frac{\mu_0}{\rho_0 D_0} \tag{2.9}$$

$$Pr = \frac{C_{P0}\mu_0}{k_0} \tag{2.10}$$

$$Gr = \frac{\rho_0^2 g_0 \Phi_0 \alpha_0 d_0^3}{\mu_0^2} \tag{2.11}$$

$$Ra = Gr Pr \tag{2.12}$$

and the electrical diffusion coefficient D_0, is approximated as (Melcher 1981):

$$D_0 = \frac{\kappa_0}{40} \text{ V}. \tag{2.13}$$

Equations (2.2)–(2.4) and (2.6) are for EHD and the equations for the RBC case are (2.2), (2.3) and (2.5). An 'EHD' underbrace indicates the source term of the

momentum equation for the case of EHD flow and the 'RBC' underbrace for the case of RBC flow.

Equations (2.2)–(2.6) are the conservation of mass, momentum with an EHD or RBC body force, space charge, energy (static enthalpy), and the Poisson equation for the voltage respectively. The reader should note that in (2.3) the EHD source term on the right-hand side is only due to an applied Lorentz force and electrostrictive and dielectrophoretic forces are negligible for the simulation parameters used here (Vazquez *et al.* 2006, 2008). The non-dimensional parameters appearing have been fully explained elsewhere (Atten 1996; Castellanos 1998).

Equations (2.2)–(2.6) are non-dimensionalized with separate scales for the fluid velocity U_0 and electrical drift velocity κE_0. In the free flow case U_0 may be scaled to κE_0 and therefore the EHD momentum conservation and space charge equations have a different form where now $Q_{ref} = Q_0$ as opposed to $Q_{ref} = \epsilon_0 V_0 / \rho_0 l_0^2$ is the reference value for charge Q (Castellanos 1998):

$$\frac{\partial}{\partial t^*}(U_i^*) + \frac{\partial}{\partial x_j^*}(U_i^* U_j^*) = -\frac{\partial p^*}{\partial x_i^*} + \frac{1}{Re_E}\frac{\partial^2 U_i^*}{\partial x_j^* \partial x_j^*} + CM^2 Q^* E_i^* \qquad (2.14)$$

$$\frac{\partial}{\partial t^*}(Q^*) + \frac{\partial}{\partial x_i^*}(U_i^* Q^*) = \frac{1}{Re_E}\frac{1}{Sc_E}\frac{\partial}{\partial x_i^*}\left(\frac{\partial Q^*}{\partial x_i^*}\right) - \left(E_i^* \frac{\partial Q^*}{\partial x_i^*} + Q^{*2}\right). \qquad (2.15)$$

The RBC source term is not included in (2.14) as the EHD free flow scaling $U_0 = \kappa E_0$ is one specific to EHD. In the RBC free flow case, U_0 is scaled to $U_0 = \sqrt{g\alpha\Delta\Phi d_0}$.

The parameter C characterizes the 'injection strength' referred to in the introduction, which governs how 'strong' or 'weak' an injection is and is defined by

$$C = \frac{Q_0 d_0^2}{D_V V_0} = \frac{\tau_d}{\tau_{SC}} \qquad (2.16)$$

where

$$\tau_d = \frac{d_0^2}{\kappa_0 V_0} \qquad (2.17)$$

$$\tau_{SC} = \frac{D_V}{Q_0 \kappa_0}. \qquad (2.18)$$

In strong injection, the electric field in the dielectric liquid is mainly influenced by the space charge distribution, and in weak injection the electric field is mainly influenced by the applied electrode voltage (Vazquez *et al.* 2008). A system is said to be under a strong injection regime if $C \gg 1$ and under a weak injection regime if $C \ll 1$. This term is the ratio of the ionic drift time scale τ_d to the Coulombic charge relaxation time scale τ_{SC} and therefore the smaller τ_{SC} is, the more intense the injection.

The parameter T, given by

$$T = \frac{D_V V_0}{\kappa \mu} = Gr_E Pr_E \qquad (2.19)$$

is the product of the electrical Grashof number Gr_E (now defined using $Q_{ref} = Q_0$) and the electrical Prandtl number Pr_E (Castellanos 1998) and may be thought of as an electrical Rayleigh number (Castellanos 1991, 1998), making it an indicator of electroconvective instability. For a strong injection case, roll structures have been calculated, through instability analysis, to appear when $T = 161$ (Castellanos 1991, 1998) while for the weak injection case the instability threshold is reached when $T = 220.7/C^2$ (Castellanos 1991, 1998). These instability thresholds have been

Value	RBC	S1	S2	S3	SP
Aspect ratio (L d^{-1})	6	6	5	5	5
Specific charge $Q_0 = Q_B$ (C kg^{-1})	—	0.0006	0.0006	0.0006	0.001
Voltage V_B (v)	—	500	500	500	1780
Viscosity ν (m^2 s^{-1})	1.75×10^{-7}	3.8×10^{-6}	5×10^{-7}	3.5×10^{-7}	1.7×10^{-6}
Density ρ (kg m^{-3})	1000	1000	1000	1000	1000
Ionic mobility κ (m^2 (Vs)$^{-1}$)	—	7.9×10^{-9}	6×10^{-8}	8.6×10^{-8}	1.8×10^{-8}
Injection strength C	—	10	10	10	4.6
Rayleigh number Ra or T	140000	500	500	500	1780
Reynolds number Re or Re_E	355	1	60	120	19

TABLE 1. Simulation parameters for all cases with distance between plates $d = 0.5$ mm and electrical permittivity $D_V = 3.03 \times 10^{-11}$ F m^{-1}. For the EHD cases (S1–S3, SP) the Reynolds number is the electric Reynolds number Re_E and the Rayleigh number $= T$ while for the RBC case Re and Ra are the conventional Reynolds and Rayleigh numbers respectively.

subsequently confirmed through computational investigations (Chicon *et al.* 1997; Vazquez *et al.* 2006, 2008); however a discrepancy exists between the experimentally measured critical $T = 100$ value for strong injection and the theoretical $T = 161$ quoted above (Castellanos 1991). The parameter T may be compared to the thermal Rayleigh number Ra in (2.12), where rather than it being the ratio of buoyancy force to diffusion force it is now the ratio of electrical force to diffusion force.

The parameter M is a measure of electrohydrodynamic turbulence in a system (Atten 1996, 1998) and is therefore related to the electrical Reynolds number Re_E, where T is defined in (2.19):

$$M = \frac{(D_V/\rho)^{1/2}}{\kappa} = \left(\frac{T}{Re_E}\right)^{1/2}, \quad Re_E = \frac{\rho\kappa V}{\mu}. \tag{2.20}$$

The value of M physically represents the ratio of hydrodynamic to ionic mobility and may be derived by equating the electrical energy to the kinetic energy and utilizing the $U_0 = \kappa E_0$ scaling. The electrical energy $((1/2)D_V E^2)$ is proportional to Re_E^2 indicating that a greater Re_E should result in more energetic eddies and wider scale range. While $(1/2)D_V E^2$ is not the rate of input of energy, it is the electrical energy which appears due to the applied field and Castellanos (1998) assumes that all of this is converted to kinetic energy, physically appearing as electroconvective motion.

2.2. *Geometry and numerical procedure*

2.2.1. *Simulation inputs*

The coordinate system used is Cartesian and two plates of area $= L \times L$ normal to the y-axis are separated by a distance d. The sides of a single control volume are referred to as w_x, w_y and w_z in the x, y and z directions respectively. Boundary conditions were chosen so as to achieve strong injection conditions. Specifically, four strong injection cases along with one RBC case with non-dimensional numbers outlined in table 1 were computed. The aspect ratio L/d was kept at the values shown in table 1 in order to ensure that the domain width is significantly larger than the theoretical roll length

(Vazquez *et al.* 2008). It should be noted that case 'strong 1' (S1) was run in two and three dimensions in order to reproduce previous two-dimesional simulations available in the literature (Vazquez *et al.* 2006, 2008). Cases 'strong 2' (S2) and 'strong 3' (S3) were run in order to investigate the effect of a higher Re_E on three-dimensional electroconvection for fixed T and C values.

The practical case 'SP' values are based on experimental studies carried out by the authors. A typical charge injection atomizer with an orifice diameter $\phi = 100\ \mu m$ and $d/\phi = 1$ as may be seen in figure 1 injects a current $I \sim 2\ \mu A$ at a voltage ~ 3000 V, and operates using diesel oil which has a typical density of 840 kg m^{-3}, and dynamic viscosity equal to 0.002 Pa s, equating to $\kappa = 1.5 \times 10^{-8}$ m^2 (Vs)$^{-1}$ (Melcher 1981). However in the simulations here, the same domain height is retained for case SP as in cases S1, S2, S3 and RBC, namely $d = 0.5$ mm. For that reason, the boundary conditions were altered, in order to achieve the same non-dimensional numbers as in the experimental case, equating to $T = 1780$, $C = 4.6$ and $Re_E = 19$. Running this practical case will not only show how a practical atomization device could be affected by turbulent EHD, but it will also illustrate the effect of a higher T in conjunction with a higher Re_E as opposed to cases S1 and S2 which contain a T value close to the instability threshold. The reader should note that simulation SP carried out here is only a first step towards understanding the complex EHD flow within a charge injection atomizer.

2.2.2. *Boundary conditions*

For the charge injection boundary an x, z plane of control volumes $(w_y > y > 0)$, the first row of control volumes next to the bottom wall boundary, are maintained at a fixed value of charge, $Q_0 = Q_B$ (C kg^{-1}) and at a fixed value of voltage, $V_0 = V_B$. The x, z boundary below this plane of control volumes, at $y = 0$, requires $dV/dy = 0$ and $dQ/dy = 0$, and the top x, z plane $(y = d)$ is a wall with boundary conditions $V = 0$ and $dQ/dy = 0$. The left and right boundaries, normal to the x and z directions are a periodic pair. The computational method agrees with the analytical solution of charge injection to within typically 3 %.

For the RBC case, the bottom wall at $y = 0$ is at a fixed temperature Φ_{HOT} while the top wall at $y = d$ is at a fixed temperature Φ_{COLD}. In contrast to the EHD simulations, boundary conditions may be applied at a wall in RBC, by virtue of a much simpler analytical solution which is not asymptotic at the wall boundaries. The no-slip condition is employed for all walls for the velocity field for both the EHD and RBC cases.

2.2.3. *Numerical method*

A parallelized version of FLUENT 6.3 was used. User defined functions were written in order to incorporate the space charge transport and the Poisson equation for the voltage, while scripts were also written to include a Lorentz source term in the momentum conservation equation in three dimensions. The simulation was carried out using a second-order implicit finite-volume scheme in both time and space. More specifically, the second-order QUICK scheme (Versteeg & Malalasekera 1995) was used to spatially discretize the momentum and space charge transport equations, while time was discretized using a second-order fully implicit method. Pressure was also discretized using a second-order method and the SIMPLE method (Versteeg & Malalasekera 1995) was used to couple the pressure and velocity fields. Second-order central schemes were used for both integration and diffusion.

Scale	RBC	S1	S2	S3	SP
Kolmogorov length η (m)	6.1×10^{-6}	7.9×10^{-5}	1.3×10^{-5}	9.7×10^{-6}	1.5×10^{-5}
Kolmogorov time τ (s)	2.0×10^{-4}	1.6×10^{-3}	3.0×10^{-4}	2.7×10^{-4}	1.3×10^{-4}
Spatial resolution	1.20η	0.09η	0.54η	0.51η	0.48η

TABLE 2. Kolmogorov microscales for all cases.

2.2.4. *Spatial and temporal resolution*

In order to acquire an initial estimate of the resolution required for the simulations the Kolmogorov scales of the problem were estimated. In RBC, the rate of dissipation is estimated via (Eckhardt, Grossman & Lohse 2007):

$$\epsilon_{dip} \sim \nu^3 d^{-4} Pr^{-2} Ra(Nu - 1). \tag{2.21}$$

An estimate for the Kolmogorov scale in EHD has been provided by Castellanos (1991) and is given by:

$$\frac{\epsilon_{dip}}{d} \sim \left(\frac{2700}{M}\right)^{3/8} \left(M\frac{T}{M^2}\right)^{-3/4}. \tag{2.22}$$

Assuming the Kolmogorov hypotheses hold this may then be used to define the hydrodynamic dissipative scales. Using the properties from table 1, the Kolmogorov length and time scales for the various cases are provided in table 2. Based on the Kolmogorov microscale estimates, and also accounting for the fact that the Courant number must be ~ 1, the spatial resolution employed in the '*y*' direction is also presented in table 2.

A non-uniform mesh was used for the strong injection simulations and mesh independence tests in both two and three dimensions confirmed sufficient spatial resolution. Although Kolmogorov scales and mesh independence testing validated the simulations it must be noted that theoretically, the simulations are not a true direct numerical simulation (DNS) by virtue of the large electrical Schmidt numbers.

The electrical Schmidt number $Sc_E = \mu/\rho D_Q$ defined as the ratio of momentum diffusivity to the charge diffusivity gives an estimate of the ratio between the electrical length scales and hydrodynamic length scales. This particular non-dimensional number, to the authors' knowledge has not been calculated or discussed in the available literature that simulates EHD flow in two dimensions. For the strong injection cases in this paper, Sc_E ranges from 163 (case S3) to 19 000 case (S1) which is very significant. This suggests that for any of the cases, a true DNS using Eulerian methods is not possible with computing power available today. Energy created on the small electrical scales close to the bottom boundary may not be transferred to the larger hydrodynamic length scales, which will inevitably create an error, especially in any higher-order moment calculations. Furthermore, fixing the charge and voltage at a row of control volumes is also theoretically incorrect, given that the values are fixed at the cell centroids located several electrical length scales away from the bottom wall. While this is an inherent problem with the simulations here, EHD simulations have been carried out in the past with large Sc_E even though such issues have not been discussed. Previous Eulerian methods such as those of Traore *et al.* (2010) proved successful in simulating two-dimensional large-scale structures, however it is uncertain how such a method would accurately calculate values of fluctuating electric field

E'_i, relevant in fully turbulent three-dimensional EHD, where E'_i by definition is a continuum variable that also exists on sub-Kolmogorov scales. As shall be shown in this paper, the electric field fluctuations are not negligible close to the walls. Given that it is demonstrated through results in §6.4 and onwards that physical phenomena are captured and validated, and budgets are reproduced within quantifiable errors, the authors assume that the significance of electric field fluctuations close to the walls is real. For further discussion on large-Sc_E simulations the reader is directed to the original work by Batchelor (1959) and more recent work by Yeung, Xu & Sreenivasan (2002), the latter dealing with Sc up to 64. In Batchelor (1959) a sub-Kolmogorov length scale is defined as $\eta_b = ((\nu D_Q)/\epsilon_{dip})^{1/4} = \eta/\sqrt{Sc_E}$, and therefore given available computing power today it is unlikely that any finite-volume method can capture the 'Batchelor' length scales for an EHD problem.

Concerning the time step, this was scaled to the Kolmogorov time scale, τ and also relevant electrical time scales (Castellanos 1998). The time steps utilized were of the order $\sim 0.1\tau$ in order to achieve the desired Courant number of 1. The reader should note that for all cases the relevant electrical time scales were larger than the calculated Kolmogorov time scales. For example, for the S1 case the smallest relevant electrical time scale is the space charge relaxation time scale equal to 4τ, for the S2 case the smallest relevant electrical time scale is also the space charge relaxation time scale at 3τ.

2.3. *Plan of results*

Having described the problem, the numerical methods and basic validation, the simulation results will now be presented and discussed. The rest of the paper is organized as follows. First, conditions for statistical stationarity are outlined. Results from two-dimensional simulations run by the authors and others are then examined (Vazquez *et al.* 2006, 2008) which validate our implementation, discretization and boundary condition choices made here. Secondly, three-dimensional results are qualitatively discussed by presenting a selection of non-dimensionalized contour plots. Thirdly, quantitative characteristics of the instabilities are discussed via examination of bivariate distributions, two-point correlations, and spectral data, the latter study being carried out in order to understand the role of kinetic and electrical energy in EHD turbulence. The paper then proceeds to discuss real-space mean and second-order moment profiles, and budgets of the turbulent kinetic energy, turbulent scalar flux and turbulent scalar variance. The second-order moment results and energy budgets are also utilized in order to investigate the scaling made by Hopfinger & Gosse (1971).

3. Statistical stationarity

A necessary condition to meet before performing averaging on turbulent flow data is for statistically stationary conditions, and here this is demonstated for the cases of table 1. Analysing the evolution of $\langle Q \rangle$ with time will illustrate this requirement while also revealing information regarding how $\langle Q \rangle$ progresses with time. $\langle Q \rangle$ here is defined as the spatial average along a plane at a fixed y position and has been non-dimensionalized with the charge level at the bottom wall Q_B. In figure 2 the evolution of temperature $\langle \Phi \rangle$ is also included, at a fixed y position in the centre and therefore $\langle N \rangle$ in the y-axis represents charge or temperature for the EHD and RBC cases respectively. The time axis has been non-dimensionalized by the theoretical eddy turnover time equal to $2\tau_d$ for the EHD case, and $\tau_{rbc} = d/(g\alpha\Delta\Phi d)^{1/2}$ for the RBC case. In order to make the plots clearer the time component of the RBC case has
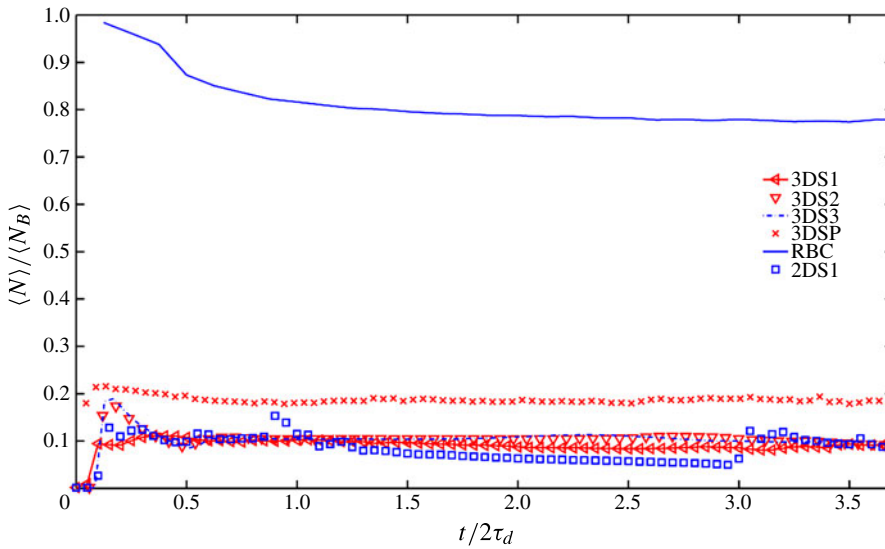
FIGURE 2. (Colour online available at journals.cambridge.org/flm) Evolution of $\langle N \rangle/N_B$ (where $\langle N \rangle$ represents $\langle Q \rangle$ or $\langle \Phi \rangle$) with τ_n at $y = 0.5d$ for all cases of table 1, where for example, 3DS1 indicates the result of a three-dimensional simulation run for case S1.

been divided by a factor of 30. This factor has been applied because the time scale associated with statistical stationarity for the RBC case is related to the mechanical diffusion time scale which is significantly larger than EHD time scales, in particular τ_{SC}. Castellanos (1991) and Atten (1996) note that the tendency for a charged 'packet' to travel from the emitting electrode (bottom) to the collecting electrode (top) is mainly counteracted by the relaxation of excess charge, and this can be seen here as the EHD simulations take much less time to reach a statistically stationary state when compared to the RBC simulation. Comparing to the S1 case as an example, the RBC mechanical diffusion time scale is $\sim 200\tau_{SC}$. The fact that the diffusion time scale is the stabilizing mechanism in RBC flow agrees with the literature (Getling 1998), and towards the early development of the RBC simulation one can see two 'kinks' corresponding to the change from a pure thermal 'conduction' case, to the onset of thermal convection and finally to the creation of RBC turbulence.

Of further interest is the fact that the value of $\langle Q \rangle$ reaches a similar stationary state when comparing the two-dimensional to the three-dimensional cases. This is because the stabilizing mechanism is present in the vertical (y) direction which is common in both the two-dimensional and three-dimensional cases.

The reader should note that throughout the paper, averaged results denoted by $\langle\langle n \rangle\rangle$ indicate the ensemble average of n, i.e. the values of n averaged along a fixed plane in both space and time. This is done by determining the mean over a number of realizations in time, while ensuring that data are sampled over a total time corresponding to at least three eddy turnovers after the simulation has reached statistically stationary conditions.

4. Two-dimensional validation

An extensive validation study of our method has been conducted by the present authors (Kourmatzis & Shrimpton 2012) and will be published separately and therefore
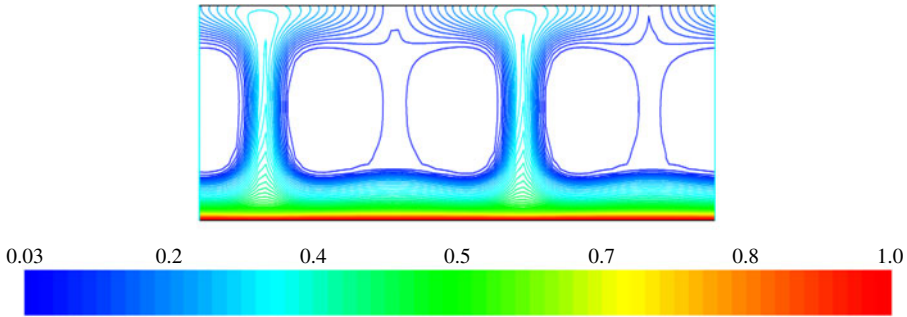
0.03			0.2			0.4			0.5			0.7			0.8			1.0

FIGURE 3. (Colour online) Normalized two-dimesional space charge distribution (Q/Q_0) for case S1 of table 1.

here we only present selected results for brevity. Two-dimensional simulation results for strong injection at values of T ranging from 160 to 500(case S1 from table 1) were run in order to reproduce simulations conducted by Vazquez *et al.* (2008) before proceeding with three-dimensional simulations. It was assumed that only bulk convection and ionic drift contribute to space charge transport (Vazquez *et al.* 2006, 2008). For strong injection, the instability threshold was found to be $T \sim 170$ where below this value no rolls were observable; however when running simulations with T above this critical value, rolls were clearly observable validating that the code correctly captures the instability threshold for the strong injection case. As observed by Vazquez *et al.* (2008) we also found a two-roll structure for the strong injection simulations at values of approximately $T = 400$–500, while the finite-volume simulation also revealed weak two-roll structures at values of $T = 200$–300 which was not noted in the particle-in-cell (PIC) method of Vazquez. *et al.* but was observed for the flux corrected transport (FCT) method.

Figure 3 shows an example of the normalized two-dimensional space charge distribution (C kg^{-1}) at $T = 500$, $C = 10$ and $Re_E = 1$ for the two-dimensional geometry (case S1 from table 1) run with $L/d = 2.4$ as utilized in Vazquez *et al.* (2008) under statistically stationary conditions. The double roll structure observed by Vazquez *et al.* (2008) is clearly visible and is unstable with time. The number of rolls varies from one to approximately seven. Furthermore, as observed by Vazquez *et al.* (2008) for the strong injection case, the majority of the charge is present on the injector surface and then sharply decreases to a minimum.

5. Qualitative three-dimensional results

This section shall directly compare the three-dimensional results of S1 of table 1 to the two-dimensional results noted in the previous section. The other strong cases of table 1 and the RBC case are then examined in order to make some first observations regarding more chaotic electroconvection in three dimensions.

5.1. *Effect of third dimension (case S1)*

Figure 4(*a*) shows the normalized velocity magnitude viewed on an iso-surface of volume-average space charge ($\langle Q \rangle_{vol}$) for strong injection. Figure 5(*a*) is a two-dimensional section of normalized space charge, at $y = 0.5d$ for the S1 case. For the strong injection case, in three dimensions irregularly shaped rolls are seen, which is observable from figures 4(*a*) and 5(*a*).
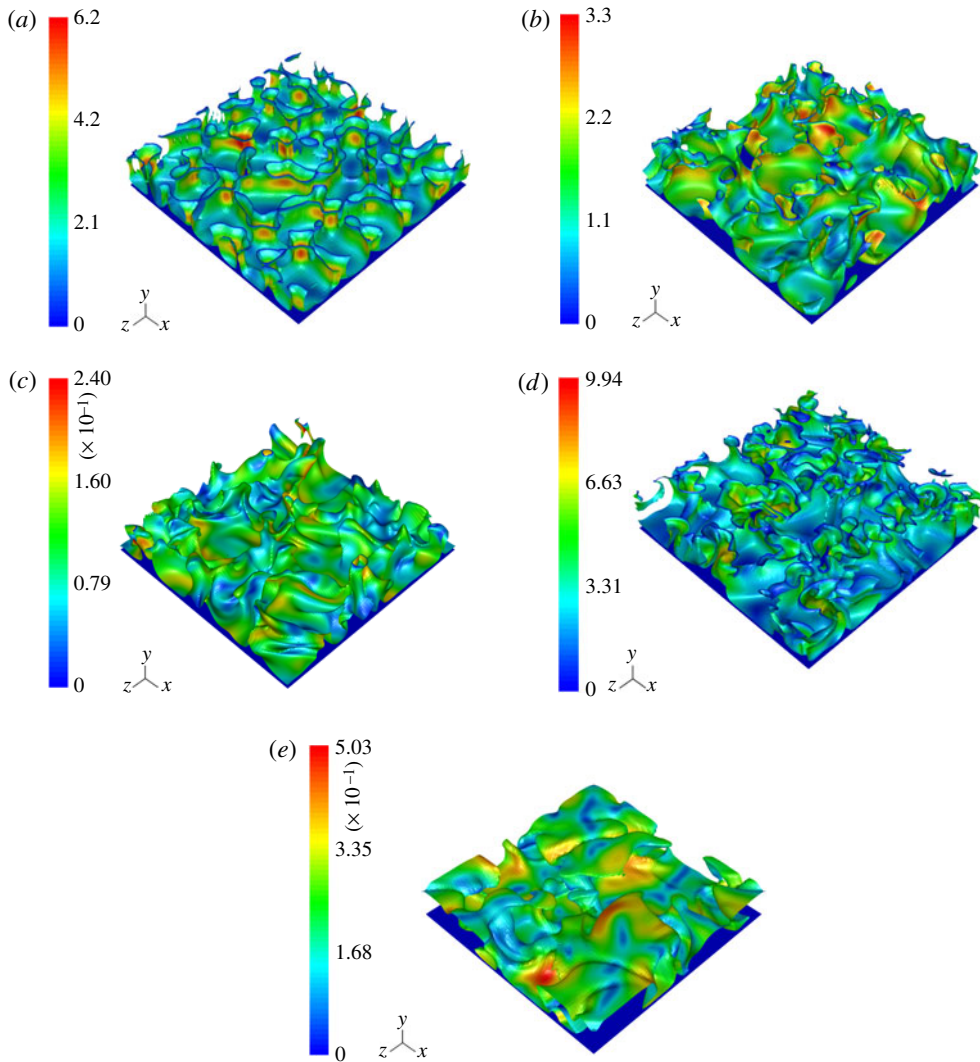
FIGURE 4. (Colour online) Normalized velocity magnitude $V_{mag}/\kappa E_0$ (*a–d*) and $V_{mag}/\sqrt{g\alpha\Delta\Phi d}$ (*e*) on $Q = \langle Q \rangle_{vol}$ or $\Phi = \langle \Phi \rangle_{vol}$ iso-surfaces for all cases of table 1: (*a*) S1 ($L/d = 6$); (*b*) S2 ($L/d = 5$); (*c*) S3 ($L/d = 5$); (*d*) SP ($L/d = 5$); (*e*) RBC ($L/d = 6$).

It is important to note that as opposed to the two-dimensional simulations of the present authors and others, through the three-dimensional results a larger range of roll structure size is observed, as the three-dimensional mixing in the domain is encouraging the formation of smaller-scale eddies which are observable within the hexagonal structures. This does suggest that certain physical mechanisms that create turbulent EHD can be captured through three-dimensional simulations, but not through the two-dimensional simulations which have been run in the past.

5.2. *Effect of Re_E (cases S1–S3 and RBC)*

Having directly compared three-dimensional to two-dimensional results for low Re_E it is now of interest to examine the structure of the EHD flow between two plates
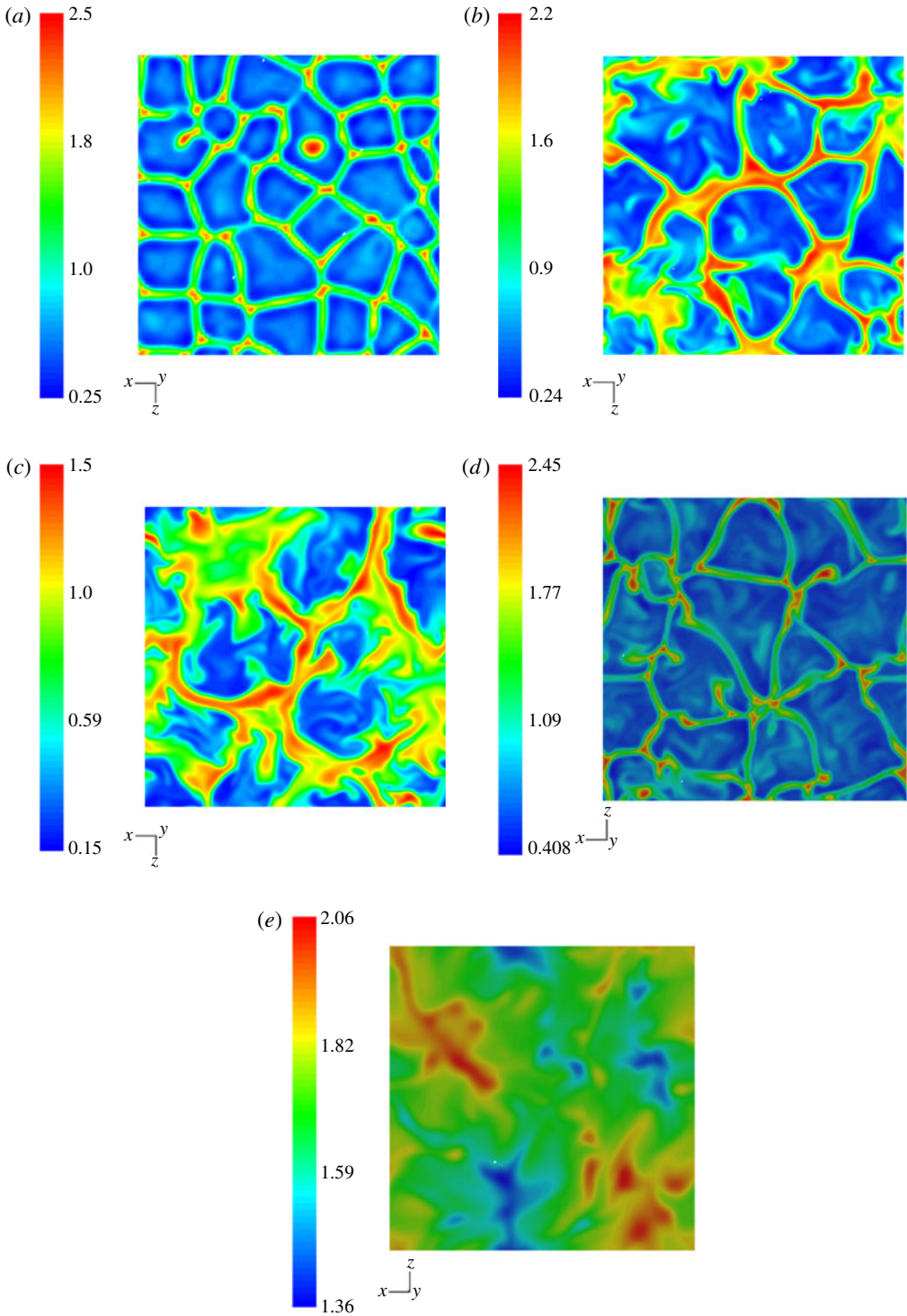
FIGURE 5. (Colour online) Normalized space charge $Q/(D_V V_0/\rho d_0^2)$ (*a–d*) and Φ/Φ_0 (*e*) for all cases of table 1 at $y = 0.5d$ (*a*) S1 ($L/d = 6$); (*b*) S2 ($L/d = 5$); (*c*) S3 ($L/d = 5$); (*d*) SP ($L/d = 5$); (*e*) RBC ($L/d = 6$).

at an elevated electric Reynolds number Re_E and compare to a high-Re RBC case, namely cases S1–S3 and RBC of table 1 are examined. A higher Re_E is of interest as we expect to see a less-stratified space charge distribution throughout the domain as the inherently three-dimensional turbulent mixing process becomes more relevant. Figure 4(*b*,*c*) shows the normalized velocity magnitude viewed on an iso-surface of volume-average space charge ($\langle Q \rangle_{vol}$) for the S2 and S3 cases respectively. While qualitatively, the structures that arise look quite similar to case S1, there is one distinct difference which shows how turbulent kinetic energy has begun to 'mix' the space charge creating more randomized structures. It is clear from figure 4(*b*,*c*) that the momentum is more evenly distributed as the non-dimensional velocity magnitude range is from 0 to 3.3 for case S2 and 0 to 0.24 for case S3 in contrast to a range from 0 to 6.2 for case S1 where the distribution is more stratified. The reader should note that for most cases the non-dimensional velocity magnitude is greater than the ionic drift velocity as stated by Lacroix, Atten & Hopfinger (1975); however here it can be seen that case S3 yields a non-dimensional velocity of 0.24. While this at first may seem a mistake, it is in direct agreement with the results of Lacroix *et al.* (1975) where for *M* values less than ∼3 it was determined that the velocity magnitude becomes smaller than the ionic drift velocity. This occurs as the electrical Nusselt number Nu_E, proportional to $M^{1/2}$ in the inertial state, approaches 1, which Lacroix *et al.* (1975) state is equivalent to a low-Pr thermal RBC case. The fact that this simulation has been able to capture this 'saturation' phenomenon shows that fully turbulent EHD has been achieved.

Observing the RBC case of figure 4(*e*) where normalized velocity magnitude is viewed on an iso-surface of volume-averaged temperature ($\langle \Phi \rangle_{vol}$) it may be seen that qualitatively, the structures look most similar to those of case S3 where the range of non-dimensional velocity magnitude is from 0 to 0.5 showing contours over a narrower range of velocity. The narrower range indicates that the roll velocity is becoming more uniform throughout the domain, thus indicating an efficient mixing of charge in the EHD case, and an efficient mixing of heat in the RBC case, and therefore the creation of homogeneity. Particularly in cases S3 and RBC of figures 4(*c*) and 4(*e*) the roll structures seem to be more random in direction when compared to cases S2 and S1. Furthermore, generally observing any of the strong injection cases and comparing to the RBC case, it is quite clear that in the RBC case the boundaries between hot and cold plumes seem to be more diffuse when compared to the strong cases of figure 5(*a*–*d*) where there are steeper gradients. The EHD boundary layer is much thinner than the thermal counterpart, which is partly responsible for the less diffuse boundaries in EHD. However, a further explanation may be provided via calculation of the electrical Prandtl number Pr_E. This may be calculated from (2.19) and for cases S1, S2, S3 and RBC Pr_E or Pr is equal to 0.09, 0.002, 0.001, and 1.1 respectively. In RBC since the ratio of viscous diffusion to thermal diffusion is approximately 1, diffuse boundaries are observable in contrast to strong EHD cases where viscous diffusion is significantly less than 'electrical diffusion'.

Further information may be gained by observing two-dimensional cross-sectional views of cases S1–S3 and RBC. It is observed that in the higher Re_E case of figure 5(*b*,*c*), the edges of the rolls have become thicker showing how the space charge field is moving towards a less stratified distribution which is also reflected in the momentum field as these two variables are intricately coupled. Through case S3 it may be seen that the area ratio of lower charge to higher charge plumes is decreasing moving to what is effectively observed in the RBC case of figure 5(*e*), a well mixed, closer to uniform, distribution of the relevant scalar variable. The range of

non-dimensional temperature in the RBC case lies between 1.36 and 2.06 as opposed to the EHD cases where we can observe a much wider spectrum of charge level. Case S3 of figure 5(*c*) shows a significant decrease in stratification where the plume thickness is seen to have increased dramatically when compared to cases S2 and S1 showing the effect of Re_E equal to 120. The reason for this decrease in stratification with an increase in Re_E is an increase in the turbulent kinetic energy when moving from case S1 to S3 as shall also be seen in § 6.5.1.

5.3. *Case SP: Effect of T*

An increased level of mixing is also visible from figure 5(*d*) where within the space charge rolls smaller scales can be seen as was also observed with cases S2 and S3; however the edges of the rolls are not as thick as in figure 5(*b*,*c*) initially indicating that Re_E is the main governing parameter responsible for length scale distribution within three-dimensional EHD convection.

   Although there are small scales present in the case SP contour plot, comparing figure 5(*d*) to any of the other strong cases one may see that case SP seems to be the most similar to case S1. While case SP has a significantly higher T value, its Re_E is less than both cases S2 and S3 and furthermore, for case SP, Pr_E is equal to 0.01, a value within the same order of magnitude as case S1 where $Pr_E = 0.09$. This indicates that although this 'practical' charge injection case has $Re_E = 20$ much greater than the $Re_E = 1$ for case S1, the fact that they have similar ratios of viscous to electrical diffusivity means that the structures are stabilized in a similar manner. From figure 4(*d*) it is again clear that cases S2 and S3 seem less stratified indicating that the higher Re_E of cases S2 and S3 have provided greater mixing when compared to case SP of figure 4(*d*). Charge injection atomizers may be operated at even higher Re_E and case SP is only one example of a 'practical' case. What is clear however, is that with a charge injection atomization device, in locations where the free-convection assumption made here holds, there will certainly be significant EHD instability which for high enough Re_E will manifest into turbulent flow. For a more detailed discussion on the internal flow of a charge injection device the reader is directed to Shrimpton & Kourmatzis (2010).

6. Quantitative characteristics of the instabilities

   In this section quantitative characteristics of three-dimensional EHD plumes are reported, and the analysis begins by analysing real-space data such as bivariate distributions and two-point correlations in order to extract further qualitative and quantitative insight while also calculating integral length scales.

6.1. *Bivariate distributions*

The bivariate probability distributions of q' versus v' (for EHD) and Φ' versus v' (for RBC), where $n' = n - \langle\langle n \rangle\rangle$, are calculated at $y = 0.5d$ in order to draw both qualitative and quantitative comparisons between the three-dimensional EHD cases and the RBC case. Here, $\langle\langle n \rangle\rangle$ is the combined spatial and temporal average of n taken along a 2D plane at a fixed *y*-position over a number of realizations under statistically stationary conditions.

   Concentrating on the RBC case of figure 6(*e*), a single mode is observed, indicating that statistically, one cannot distinguish between those rolls travelling from the hot to the cold wall, and then those travelling back down, which is a sign of conventional buoyancy-driven turbulent flow. The RBC data of figure 6(*e*) are almost completely
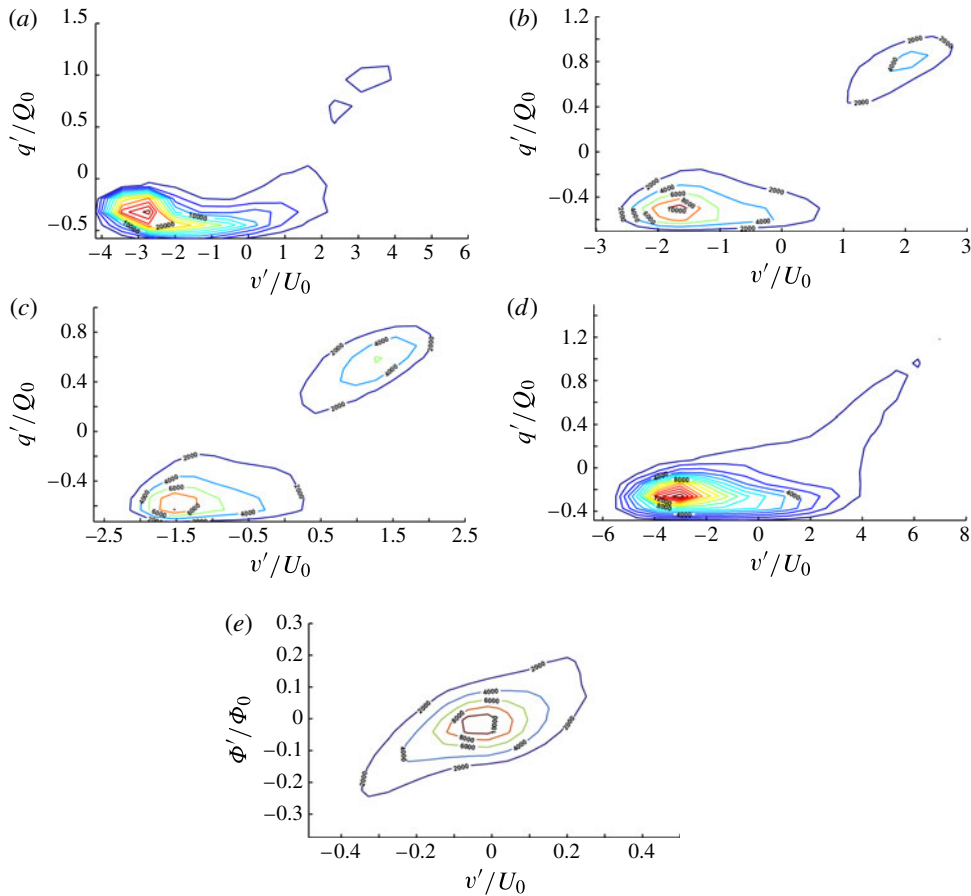
FIGURE 6. (Colour online) Bivariate distributions of non-dimensional vertical (*y*-direction) velocity fluctuations v'/U_0 and scalar fluctuations q'/Q_0 or Φ'/Φ_0 for all cases of table 1 at $y = 0.5d$ where contours represent the total number of binned samples; where here $Q_0 = D_V V/\rho d_0^2$ and Φ_0 is given by $\Phi_{HOT} - \Phi_{COLD}$; $U_0 = \kappa E_0$ for EHD and $U_0 = \sqrt{g\alpha\Delta\Phi d_0}$ for RBC: (*a*) S1; (*b*) S2; (*c*) S3; (*d*) SP; (*e*) RBC.

symmetric and the result here compares with probability distributions of turbulent flow in the literature (Pope 2000). The dominant peak of this system occurs where both v' and Φ' are approximately equal to zero, unlike the EHD cases, the latter revealing that the bivariate distributions are skewed or bi-modal. We now compare the EHD distributions as Re_E increases, as this can give us qualitative information regarding mixing and turbulent statistics.

Concentrating on the bivariate distributions of cases S1–S3 of figure 6(*a*–*c*), as Re_E increases the probability distribution become more symmetric, moving closer to the distribution shown in figure 6(*e*). However unlike in RBC, there is a bimodality present which also agrees with figures 4(*a*–*c*) and 5(*a*–*c*) where some ordered upward and downward travelling plumes are present. Observing case S1 it may be seen that there is a very high probability at a single point, and a long tail is formed at lower probabilities indicating the high skewness present. As Re_E increases however, this skewness is no longer present, and when moving from case S2 to S3 the

difference in probability between the two peaks decreases, indicating that the upwards and downwards travelling plumes are beginning to mix. Observation of case SP of figure 6(*d*) reveals that severe asymmetry is observable, though a pronounced bimodality is not present, making this distribution bear more similarity with the bivariate distribution of case S1. The reason for this is the similar Pr_E between these two cases, as outlined in § 5.

6.2. *Two-point correlations*

Two-point correlations of the velocity field calculated in one and two dimensions are reported for the three-dimensional results, and we compare the one-dimensional two-point correlations from the three-dimensional results to the two-dimensional results in order to draw basic conclusions regarding length scales. Spatial integral measures that arise from them are examined via calculation of the longitudinal velocity correlation R_{22} given by:

$$R_{22}(r, x) = \frac{\langle\langle u_2(x)u_2(x+r)\rangle\rangle}{\langle\langle u_2(x)u_2(x)\rangle\rangle} \tag{6.1}$$

where r is a displacement in the x, z plane.

For the one-dimensional correlation calculation from the three-dimensional simulations (3D1D), R_{22} is calculated at a fixed z and y position along an x direction, while the two-point correlation calculated from two dimensions (3D2D) applies (6.1) in both the x and z directions, again at a fixed y position. The one-dimensional two-point correlation results from the three-dimensional simulations described above (3D1D) will be compared to two-point correlations in one dimension from the two-dimensional simulations (2D1D), calculated at the same y position, and this will further elucidate the effect of adding an extra dimension. Here, the effect of three-dimensional EHD will be examined through length scale distribution and will support the qualitative observations made in § 5.

The 3D1D result for the strong injection cases is calculated along a line of constant $z = 3d$ (halfway along the domain in the z direction $= 6d/2$, where the aspect ratio $L/d = 6$) and this is determined at $y = 0.5d$. These calculations are presented alongside 1D two-point correlation results from two-dimensional simulations (2D1D) all at $y = 0.5d$.

The integral length scale, indicating the typical eddy size is defined:

$$L_{22}(x) = \frac{1}{R_{22}(0, x)} \int_0^\infty R_{22}(e_2 r, x)\, \mathrm{d}r \tag{6.2}$$

where e_2 is the unit vector in the x_2 or y direction.

Some immediate differences between the 2D1D and 3D1D two-point correlations are observed in figure 7. All of the correlations taken from the three-dimensional simulations are broader than the two-dimensional ones, indicating that there are more length scales present. Furthermore, the 3D1D R_{22} values are less correlated as r increases, when compared to the 2D1D curves, indicating that when correlating from two-dimensional simulations in one dimension, roll structures are more similar in space.

The 3D2D curve provides a greater sampling size, which results in a more realistic R_{22} curve. The integral scale, or the area under the R_{22} curve before the plot crosses zero, for the strong injection case S1 (3D2DS1) is equal to $0.24d$ and this also agrees with the qualitative information presented in figure 4(*a*).
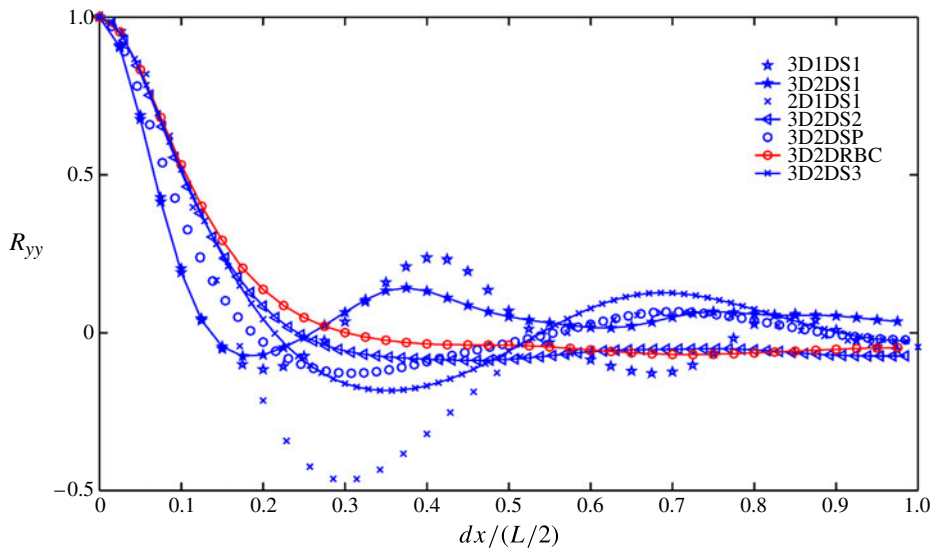
FIGURE 7. (Colour online) Two-point longitudinal velocity correlations for two- and three-dimensional simulations for all cases at $y = 0.5d$ where 1D, 2D and 3D denote one- two- and three-dimensional, respectively, and 'Sn' = Strong case n of table 1.

Let us now concentrate on the 3D2DS2 or S2 results, the 3D2DS3 or S3 results and the 3D2DSP, or SP results. Observing these curves in figure 7, it is quite clear that the higher Re_E cases are producing a larger range of roll structure size as they have a much broader R_{22} curve than 3D2DS1. Furthermore, as with conventional turbulent simulations and the RBC case (3D2DRBC), the 3D2D S2, S3 and SP curves show little correlation after crossing the $R_{22} = 0$ point, indicating that there is little spatial repeatability at larger scales throughout the domain unlike case S1. This shows that there is energy present over a range of scales, since electro-inertial momentum transfer $\rho \kappa V$ is now much larger than μ. Although cases S1 and SP showed similarities in the bivariate distributions and contour plots presented earlier, it is clear now that inside the larger plumes of case SP (figure 5d), more energetic smaller scale eddies are present than in case S1.

Furthermore, realizing that the 3D2D S2 and S3 curves are very similar to the RBC curve of figure 7 it may be stated that in EHD a much lower Reynolds number is required in order to achieve hydrodynamic turbulent mixing, and judging by these data, it may be said that strong cases S2 and S3 seem to be the only cases that are strictly in a hydrodynamic turbulent regime, as opposed to just in an unstable regime showing, as in §§ 5.2 and 5.3 that a higher Re_E does promote EHD turbulence. Lacroix *et al.* (1975) state that a combination of M and Re_E can promote turbulence; however in this study a single variable was investigated; in future computational studies it may be of interest to examine how length scale distributions change in three dimensions while increasing the value of $MRe_E = T/M$.

6.3. *Spectral analysis*

Having presented and discussed real-space quantities it is now of interest to analyse energy and dissipation spectra. First, this will allow a direct comparison between the EHD cases and RBC case, providing further understanding pertaining to differences

and similarities between the two areas of physics. Secondly, it will provide insight regarding how energy is distributed amongst wavenumbers for different EHD regimes, i.e. for lower- and higher-Re_E problems. Presenting the plots as compensated spectra will also allow comparison with conventional turbulent problems in the literature (Pope 2000).

For simplicity here, the turbulent kinetic and electrical energies are taken to be only attributed to $k = \rho \langle\langle u_2'^2 \rangle\rangle$ and $k_e = D_V \langle\langle E_2'^2 \rangle\rangle$ respectively, as this is the dominant direction. The spectrum is determined by taking the Fourier transform of U_2 or E_2, multiplying by the complex conjugate, and summing the energy contribution $E(K)$ from each discrete node in the x and z directions, where K is the wavenumber defined by $2\pi/L$ and takes values in the range $nK_0 - K_0/2 \leqslant |K| \leqslant nK_0 + K_0/2$; more detailed information regarding spectral analysis may be found in Castro (1989). The dissipation spectrum for the turbulent kinetic energy may then be defined using E(K) as $D(K) = 2\nu K^2 E(K)$. The reader should note that theoretically, there is no conventional dissipation spectrum for the turbulent electrical energy, and the reason for this is described now.

The equation for the turbulent electrical energy in a form suitable for the electroconvection between two plates was originally presented by Hopfinger & Gosse (1971) and is displayed here in a slightly different form:

$$\frac{\partial k_e}{\partial t} + (\overline{u_i' E_i'}\,\overline{Q} + \overline{q' u_i' E_i'}) - \underbrace{\frac{D_V}{\rho}\frac{\mu}{Sc_E}\frac{\partial \overline{q' E_2'}}{\partial x_2}}_{diff} = -\rho\kappa(\overline{E_i}\,\overline{q' E_i'} + \overline{E_i'^2}\,\overline{Q} + \overline{q' E_i'^2}). \quad (6.3)$$

The term labelled '*diff*' was neglected by Hopfinger & Gosse (1971) as it was assumed that all turbulent electrical energy is converted to turbulent kinetic energy. Here, the diffusion term '*diff*' is many orders of magnitude less than any of the other terms. It is clear that as D_V and μ are small and Sc_E is large as stated in §2.2.4, this term will be negligible. However, following from the discussion in §2.2.4 concerning the large Sc_E, assuming this term is non-dimensionalized to the sub-Kolmogorov 'Batchelor' electrical length scales then it may become more significant. As was stated however, these scales are not resolved.

Furthermore, it should be noted that the only term appearing in (6.3) which is always negative, is $-\rho\kappa \overline{E_i^2}\,\overline{Q}$, and calculation of this term from DNS yielded no conclusive evidence that this fully balances any produced energy, and this is probably attributable to fluctuations in the electric field occurring at sub-Kolmogorov length scales. Turbulent electrical energy 'dissipation' as a concept is not further discussed here, as the majority of electrical energy is converted to kinetic energy as shall be seen in §6.5.1, and thus we only concentrate on the production of turbulent electrical energy, and draw conclusions regarding its conversion to kinetic energy. The dissipation of kinetic energy is also discussed, as it is a well-defined quantity, and fully resolved.

6.3.1. *Energy spectra*

Observing figure 8(*a*) it can be seen that the general shape of the energy spectrum follows the literature for a 'turbulent' problem, with an increase in Re generally moving the peak in the spectrum to lower values of $K\eta$, where η is the Kolmogorov length, and it is further observed that using the compensated scaling, the S2 case seems to be broadest, while case SP also covers a wide range of wavenumbers indicating a varied scale size. One would expect case S3 to be broadest, however
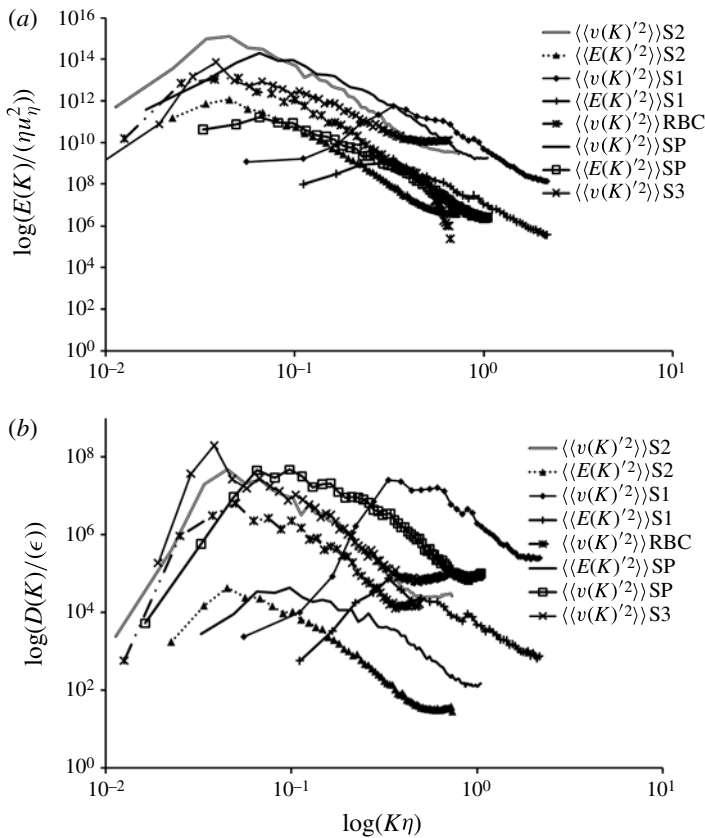
FIGURE 8. Compensated turbulent kinetic and electrical energy (*a*) and dissipation spectra (*b*) on log–log scale for all strong EHD cases and for the RBC case of table 1 at $y/d = 0.5$ where v in the figure is equivalent to u_2.

as will be seen in § 6.3.2, the S3 case has significantly more dissipation. Comparing the $\langle\langle v'^2 \rangle\rangle$ S2, S3 and SP cases it is noted that the spectrum at high $K\eta$ or at the dissipation range, is of similar magnitude $E(K)$. As in conventional turbulent flows it is seen that the hydrodynamic energy of cases S2 to SP crudely follows what a model Taylor spectrum does with an increase in Re, namely a shift in the peak to lower $K\eta$ while the energy dissipation range remains constant, and interestingly, this is also observed for the electrical energy spectra.

For the RBC spectrum curve, it is observed that the peak is shifted to the lower-wavenumber range when plotted on a compensated *x*-axis indicating that it is one of the more turbulent cases as may also be seen from table 1. The shape of the curve closely follows conventional turbulent flows, while it also resembles spectral distributions for RBC flows (Wu *et al.* 1990). For any of the EHD cases presented, comparing the turbulent kinetic to electrical energy spectra, it may be seen that the turbulent kinetic energy has a broader curve though the general distribution of energy amongst the wavenumbers seems to be similar, with a peak at the lower wavenumbers. It is of particular interest to note that an increase in Re_E not only shifts the kinetic energy spectrum to lower wavenumbers, but it also shifts the electrical

energy spectrum. This indicates that Re_E has an effect on how the turbulent electrical energy is distributed amongst the scales, showing that a change in hydrodynamic conditions will also have an impact on the electrical energy, even though turbulent kinetic energy is dominant at higher Re_E, as shall be seen in § 6.5.1. A change in hydrodynamic conditions will affect the electric field distribution because charge, velocity and electric field are all intertwined. The charge distribution is driven both by a hydrodynamic component U_i and an ionic drift component κE_i; and through Gauss's law, the charge will directly affect the electric field distribution.

It is of further interest to compare the energy spectra as a function of vertical height y/d shown in figure 9(a), and this is done here by examining the energy spectrum at a position close to the bottom wall at $y = 2w_y$ and at $y = 0.5d$ for case S2 of table 1. The spectrum for the turbulent kinetic energy is clearly of greater magnitude for all wavenumbers as one observes data further from the bottom wall. The opposite is observed for the turbulent electrical energy where the magnitude is greatest for all wavenumbers closer to the bottom wall. This further exposes how the energy is converted from an electrical origin to hydrodynamic energy as the plumes accelerate away from the bottom boundary, and this energy is converted over all of the wavenumbers.

6.3.2. *Dissipation spectra*

Attention is now drawn to figure 8(b). Observing the dissipation spectrum of the turbulent kinetic energy for any of the cases, it is seen those with the largest viscosity, such as case S1 peak at larger values of $K\eta$ though the particular curve covers a narrower range of scales showing that it is less turbulent.

From these plots information regarding where the energy is dissipated may be extracted in terms of scale size, and this was calculated by plotting $D(K)$ as a function of K as opposed to $K\eta$ (not shown here). As an example, the dissipation of kinetic energy for case S2 is utilized in order to extract the value of $L = 2\pi/K$ where $D(K)$ is significant. The dissipation curve for the fluid turbulent kinetic energy case broadens over a range of scales, the mid-point of which is at approximately $L = 33\eta$ or $0.6d$, suggesting that for the kinetic energy, the motions responsible for dissipation are in what are referred to as the 'inertial' range of scales, as is observed in a Taylor model spectrum.

From figure 9(b) similar observations are made as for the energy spectrum case of figure 9(a), though what may be seen is that for the two curves, the rate of decrease of $D(K)$ as a function of $K\eta$ is less than in the energy spectrum case, showing that the energy is dissipated at large values of $K\eta$ corresponding to smaller length scales.

The results are qualitatively very plausible as it is to be expected that turbulent kinetic energy becomes less dominant near the wall. As stated by Castellanos (1998), the only energy going into such a problem is the turbulent electrical energy, which should be converted to turbulent kinetic energy in the bulk, and this has been observed here over the full range of wavenumbers.

6.4. *Mean profiles*

While length scale, correlation and spectral information does reveal some details regarding the nature of the EHD 'turbulence' further insight can be acquired by examination of the spatial distribution of key variables across the domain, in the vertical direction. The distribution of $\langle\langle Q \rangle\rangle$ and $\langle\langle E_2 \rangle\rangle$ along y for the various cases will tell us how Re_E, T and C affect key electrical mean quantities.
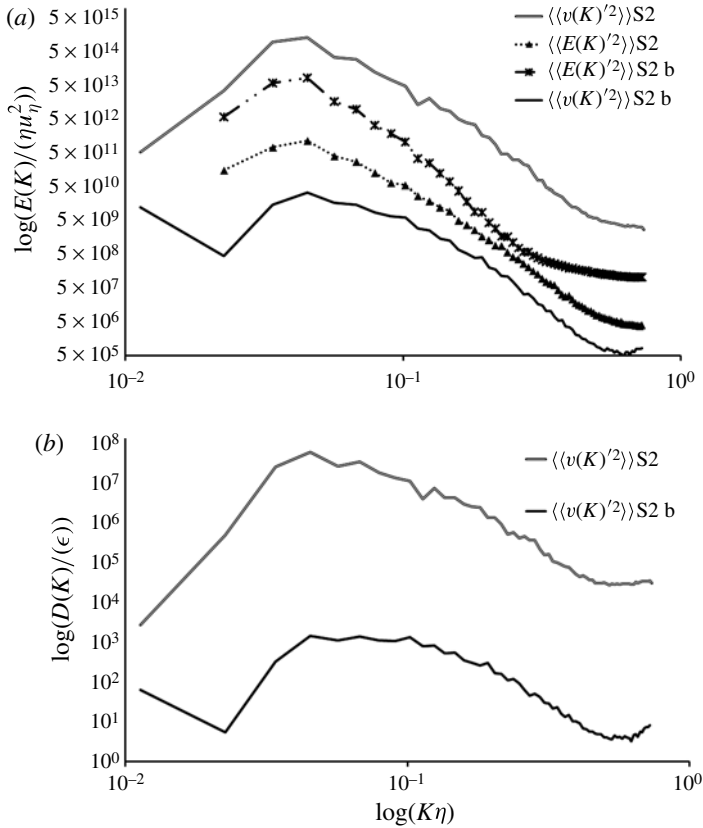
FIGURE 9. Compensated turbulent kinetic and electrical energy (*a*) and dissipation spectra (*b*) on log–log scale, at the domain mid-height $y/d = 0.5$ and at the bottom (labelled b on the figure) at $y = 2w_y$ for case S2 of table 1.

The reader should note that the method of averaging employed for the mean and second-order moments is the same as that employed for the two-point correlation calculations, outlined in §§ 6.1 and 6.2. Any fluctuating quantity n' as stated previously is equal to $n - \langle\langle n \rangle\rangle$. Prior to presenting results it is useful to state the relevant mean RANS equations of the problem, namely the mean momentum, static enthalpy, and charge equations respectively, in a commonly presented dimensional form:

$$\frac{\partial \rho \overline{U_i}}{\partial t} + \frac{\partial}{\partial x_j}\left(\rho \overline{U_i}\,\overline{U_j}\right) + \frac{\partial}{\partial x_j}\left(\rho \overline{u_i' u_j'}\right)$$
$$= -\frac{\partial \overline{P}}{\partial x_i} + \mu \frac{\partial}{\partial x_j}\left(\frac{\partial \overline{U_i}}{\partial x_j}\right) + \underbrace{\rho(\overline{E_i}\,\overline{Q} + \overline{E_i' q'})}_{EHD} + \underbrace{\rho g_i \alpha(\overline{\Phi} - \Phi_0)}_{RBC} \qquad (6.4)$$

$$\frac{\partial \rho C_P \overline{\Phi}}{\partial t} + \frac{\partial}{\partial x_i}\rho C_P(\overline{\Phi}\,\overline{U_i} + \overline{\Phi' u_i'}) = \frac{\mu}{Pr}\frac{\partial}{\partial x_i}\frac{\partial}{\partial x_i}\overline{\Phi} \qquad (6.5)$$

$$\frac{\partial \rho \overline{Q}}{\partial t} + \rho \frac{\partial}{\partial x_i}(\overline{Q}\,\overline{U_i} + \overline{q' u_i'}) + \underbrace{\rho \kappa \frac{\partial}{\partial x_i}(\overline{Q}\,\overline{E_i} + \overline{q' E_i'})}_{drift} = \frac{\mu}{Sc_E}\frac{\partial}{\partial x_i}\frac{\partial}{\partial x_i}\overline{Q} \qquad (6.6)$$
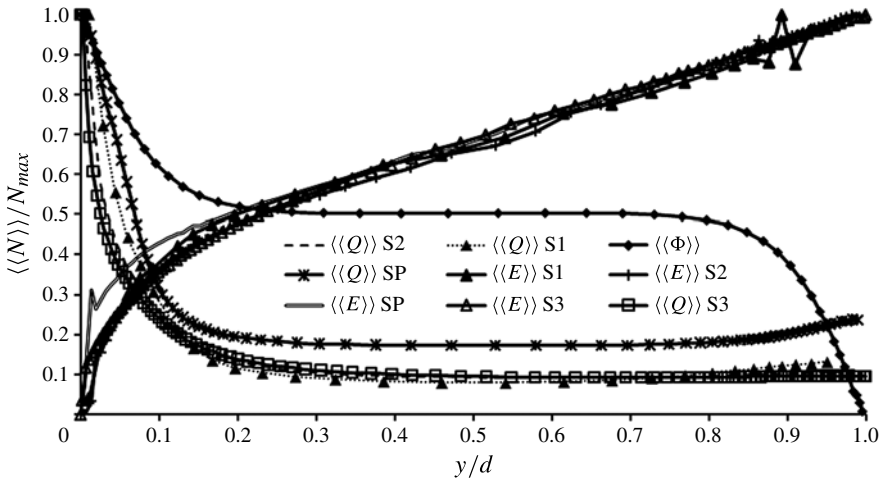
FIGURE 10. $\langle\langle Q \rangle\rangle$, $\langle\langle E_2 \rangle\rangle$ and $\langle\langle \Phi \rangle\rangle$ versus vertical position for all cases of table 1.

where the term '*drift*' may be re-written as:

$$\rho \kappa \frac{\partial}{\partial x_i} \left(\rho \frac{\overline{Q}\,\overline{Q}}{D_V} + \overline{E}_i \frac{\partial}{\partial x_i} \overline{Q} + \frac{\rho \overline{q'^2}}{D_V} + \overline{E'_i \frac{\partial}{\partial x_i} q'} \right). \tag{6.7}$$

A particularly important feature of the equations is the nonlinear ionic drift term seen from (6.6) and (6.7) which was previously discussed in an instantaneous form. The bulk convective scalar flux, which appears as $\overline{q'u'_i}$ in (6.6) and $\overline{\Phi'u'_i}$ in (6.5) is common between the RBC and EHD equations. However, upon decomposing and averaging the space charge equation it may be seen that the mean equation for charge reveals a dependence on the scalar fluctuating variance of charge $\overline{q'^2}$ as opposed to the static enthalpy equation that has no relation to its variance. This relation arises through Gauss's law for the electric field and shows how the scalar variance of charge is of particular importance in EHD, and may also be used to describe why the mean profiles of charge and temperature differ greatly, as shall be seen in figure 10.

As Vazquez *et al.* (2008) observed in two dimensions, a sharp decrease in the mean charge profile occurs on moving away from the bottom wall for all the strong injection cases as may be seen in figure 10. This is what occurs in the analytical case also; however the presence of a flow moves charged carriers away from the wall making the space charge distribution less nonlinear close to the wall. Comparison is firstly drawn between the $\langle\langle Q \rangle\rangle$ versus y/d profiles for strong cases S1, S2 and S3. Here, for the same C and T values the lower-Re_E case S1 has a charge that decreases nonlinearly from the bottom wall and then slightly increases again at $y/d = 1$. This phenomenon was also observed by Vazquez *et al.* (2008) in two dimensions, and is also observed for our strong case S3. The reason for this occurrence is that charge accumulates at the edges of the rolls and is 'thrown' around to the top side of the rolls. For the higher Re_E cases S2 and S3, this phenomenon is non-existent because charge is no longer as strongly accumulated at the edge of the rolls because of mixing, which was also visible in figure 5(*b*). For the practical strong case SP, the 'kink' at $y/d = 1$ is even more pronounced, but the charge at the bottom wall also decreases less rapidly, which is attributed to the lower C for strong case SP making it a medium to strong injection

as opposed to the purely strong injection cases of S1, S2 and S3. Self-similarity is clearly present for this range of Re_E, which shows that even with a drastic increase in input energy, mean electrical quantities remain fairly unchanged.

There is almost no observable difference in the strong mean $\langle\langle E_2 \rangle\rangle$ profiles, and even if they are normalized to V_B/d, the same trend is observed, which indicates that a more chaotic flow field has a negligible effect on the mean electric field distribution, as $\langle\langle E_2 \rangle\rangle$ is defined by the nonlinear space charge profile as opposed to any changes in the hydrodynamic behaviour of the system. In the case of RBC the key mean variable is now $\langle\langle \Phi \rangle\rangle$, and the evolution of this variable is quite different as there is no strong nonlinearity present, which is due to the absence of an ionic drift term in the governing equation for the temperature.

While the mean profiles have given some insight regarding how key variables evolve, they have not shown any significant differences between the various cases, and a better understanding can be acquired by examining higher-order averaged moment distributions.

6.5. *Second-order moment profiles*

In this section four key second-order terms are examined. The turbulent kinetic energy (k) or $(1/2)\rho\overline{u_i' u_i'}$, the turbulent electrical energy (k_e) or $(1/2)D_V\overline{E_i' E_i'}$, the turbulent scalar flux term or $\overline{q'u_2'}$ which appeared in (6.6), and the turbulent scalar variance or $\overline{q'q'}$ which also appeared in (6.6). The turbulent kinetic energy is examined in order to draw conclusions regarding how turbulent energy is produced and transported in EHD when compared to RBC.

6.5.1. *Turbulent energy*

According to Hopfinger & Gosse (1971), any term containing a fluctuating electric field component is negligible which suggests that k_e itself is negligible along with any other terms in the governing EHD equations that contain an E_i' term (Hopfinger & Gosse 1971). In order to examine the validity of the claim in our problem, k and the ratio k_e/k across the domain are plotted for all of the EHD cases.

First, profiles of k for the various EHD cases and for the RBC case are examined. Figure 11(*a*) shows k normalized by its maximum, in order to more clearly elucidate differences between the EHD and RBC cases. As in RBC, k increases away from the wall as the roll velocities increase and then reaches a peak in the middle; however in RBC k is fairly constant in the bulk of the domain. This near constant k in the bulk is not observed for the S1 case; however with the S2, S3 and SP cases it is seen that the curves are broadening when compared to the S1 case showing that at higher Re_E, EHD chaos is distributing the kinetic energy more evenly throughout the bulk, bringing it closer to the RBC distribution of energy. Of particular interest is case S3 in figure 11(*a*) where it is seen that the distribution of k is almost symmetric throughout the domain indicating a greater presence of mixing. Though it is not seen in figure 11(*a*) the reader should note that case SP produced the highest k magnitude. This indicates that the SP case should have a wide range of length scales which was observable from the spectral data; however, even though case SP has a larger magnitude of k the reader should recall that its length scale distribution as observed from figure 7, is not as varied as in cases S2 and S3 which were run at a higher Re_E. The lower scale size distribution of case SP has been attributed to the Pr_E value of this system which is similar to case S1, resulting in high input electrical energies but also proportionally high levels of stabilization not allowing as random a length scale distribution as cases S2 and S3.
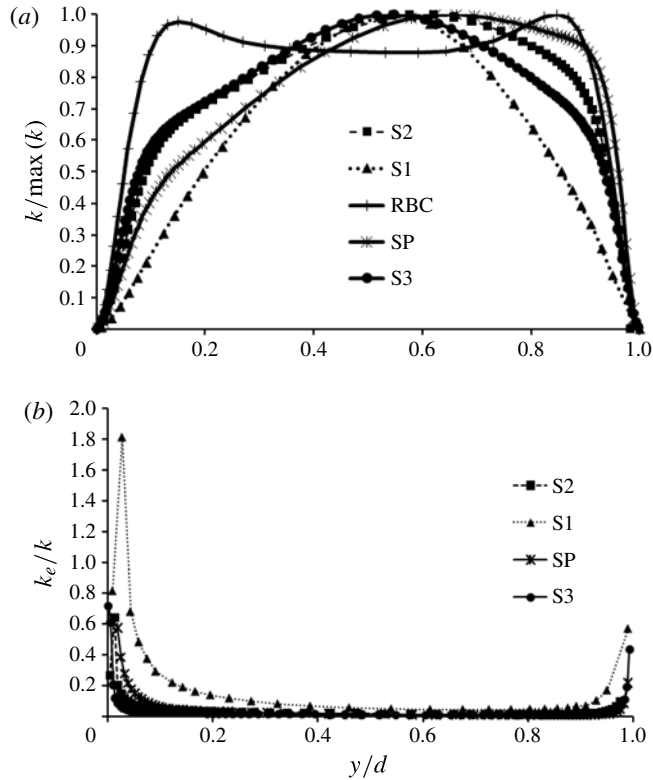
FIGURE 11. (*a*) Real-space non-dimensional turbulent kinetic energy for all cases of table 1 and (*b*) turbulent electrical energy to turbulent kinetic energy ratio for the strong EHD cases of table 1.

There is clear self-similarity throughout the various cases and also similarity of EHD and RBC even at the second-order averaged level. This shows that even though mean profiles between RBC and EHD are quite different, their hydrodynamic turbulent kinetic energy is distributed in a very similar way, showing to a certain extent that the physical characteristics of the rolls of the two cases are also similar in a statistical sense. This is a promising result as it indicates that models applicable in parallel-plate RBC should be applicable in parallel-plate EHD as well. This further shows that even though EHD has a spatially and temporally variant potential energy gradient as opposed to the RBC case where it is a constant, the hydrodynamic energy is fairly homogeneous throughout the bulk. However, in the RBC case, the energy is almost perfectly symmetric and therefore much more predictable when compared to the various strong cases which tend to be slightly skewed.

Having discussed distributions of k it is prudent to compare the curves to the k_e distributions and therefore investigate the validity of Hopfinger & Gosse's assumption outlined in § 1. Attention is drawn to figure 11(*b*) where it is observed that especially close to the bottom wall, for all of the EHD cases k_e is not negligible where for the S1 case $k_e \sim 1.8k$, for the S2–SP cases $k_e \sim 0.7k$, and for the W case $k_e \sim 0.2k$. The assumption that E' and $\overline{E'^2}$ are negligible is also of dubious validity at the top wall where the $k_e \sim 0.2k$. This finding however does not invalidate Hopfinger & Gosse's assumption as in the centre of the domain, k is indeed dominant over k_e; however
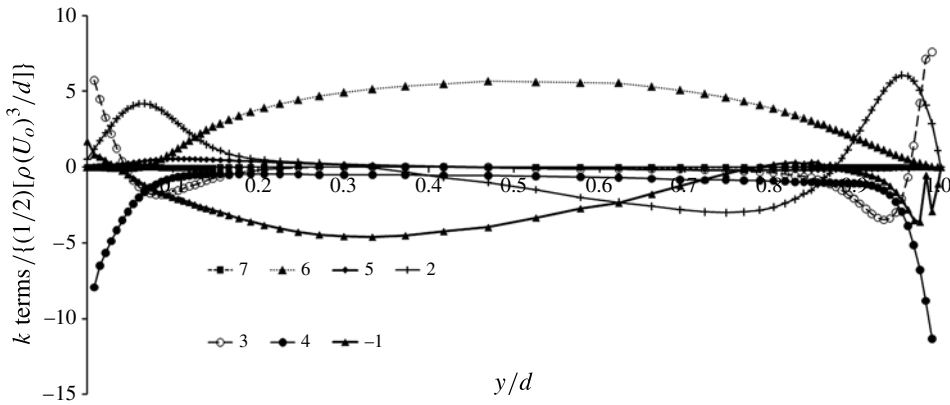
FIGURE 12. Budget of k for S2 case of table 1 as a function of y/d.

for low-Re_E cases it is not small enough to be neglected as it is still $0.2k$. As Re_E increases, the Hopfinger & Gosse high-Re_E assumption becomes more valid, meaning that the claim that $k_e \ll k$ is also validated, but only when sufficiently far from the walls.

6.5.2. *Turbulent kinetic energy budget*

The distribution of turbulent kinetic energy provides some insight into self-similarity; however it is also of interest to examine the budget of this quantity, mainly in order to examine how EHD terms contribute to the production and transport of turbulent kinetic energy. The turbulent kinetic energy, neglecting mean flow and electrostriction and realizing that there are no gradients in the $i = 1, 3$ direction, may be expressed as follows (Hopfinger & Gosse 1971):

$$\frac{\partial k}{\partial t} + \underbrace{\frac{\partial \rho \overline{\frac{u_2' u_i' u_i'}{2}}}{\partial x_2}}_{1} = -\underbrace{\frac{\partial \overline{p' u_2'}}{\partial x_2}}_{2} + \underbrace{\mu \frac{\partial^2 k}{\partial x_2^2}}_{3} - \underbrace{\mu \overline{\left(\frac{\partial u_i'}{\partial x_2}\right)^2}}_{4}$$

$$+ \underbrace{\rho \overline{Q} \, \overline{u_i' E_i'}}_{5} + \underbrace{\rho \overline{u_i' q'} \, \overline{E_i}}_{6} + \underbrace{\rho \overline{u_i' q' E_i'}}_{7}. \qquad (6.8)$$

The novel terms are the averaged EHD body force terms 5, 6 and 7 in (6.8). According to the assumption by Hopfinger & Gosse (1971) terms 5 and 7 should be negligible throughout the majority of the bulk leaving term 6 as the only contributing EHD term.

Figure 12 plots terms 1–7 from (6.8) as a function of y/d for a selected turbulent case, namely S2 as this proved to be the closest to the RBC case from figure 7. The reader should note that the turbulent transport term (term 1) was calculated from the production, pressure transport, dissipation, and molecular diffusion terms (term 1 = term 2 + term 3 + term 4 + term 5 + term 6 + term 7). The term may also be calculated directly, and more details on direct calculation of turbulent transport terms shall be presented in §6.5.4. Close to the wall the budget is a balance between molecular diffusion and dissipation as is the case in RBC (Kerr 2001) and throughout the bulk of the domain the production term is counteracted by dissipation

and transport. The only contributing production term in this instance is term 6, or the turbulent scalar flux acting on the mean electric field $\overline{q'u'_2}\,\overline{E_i}$. Furthermore, those EHD terms that contain E'_i (terms 5 and 7) are negligible in this instance, and as in RBC, the production term is the turbulent scalar flux term (Kerr 2001). Therefore, through examination of this budget it may be stated that the assumption by Hopfinger & Gosse (1971) is correct, and it is correct to claim that interactions between fluctuating electric field and velocity or space charge have a negligible effect on the distribution of turbulent kinetic energy. However, when discussion of the k_e/k profile was undertaken in §6.5.1 it was mentioned that close to the wall, $\overline{E'^2_i}$ is significant, though in the k budget, it is seen that terms containing E'_i are negligible.

Finally, the reader should note that the profiles of terms 1–7 bear extreme similarity with what is observed in RBC turbulent kinetic energy budgets (Kerr 2001) acting as a point of confirmation that the simulation physics is able to capture higher-order moment distributions accurately.

6.5.3. *Turbulent scalar flux budget*

The only flux term budget equation that is analysed here is the transport equation for the turbulent scalar flux given by the term $\overline{q'u'_2}$, which also appeared in (6.6):

$$\frac{\partial \rho \overline{u'_2 q'}}{\partial t} + \rho \underbrace{\overline{u'_2 u'_2} \frac{\partial \overline{Q}}{\partial x_2}}_{1} + \underbrace{\frac{\partial \rho \overline{u'_2 u'_2 q'}}{\partial x_2}}_{2}$$

$$+ \rho\kappa \left[\underbrace{\overline{u'_2 q'} \frac{\rho \overline{Q}}{D_V}}_{3} + \underbrace{\overline{u'_2 E'_2} \frac{\partial \overline{Q}}{\partial x_2}}_{4} + \underbrace{\frac{\partial}{\partial x_2}(\rho \overline{E_2}\,\overline{q'u'_2})}_{5} + \underbrace{\frac{\partial}{\partial x_2}\overline{u'_2 q' E'_2}}_{6} \right]$$

$$= -\underbrace{\overline{q' \frac{\partial p'}{\partial x_2}}}_{7} + \left(\mu + \frac{\mu}{Sc_E}\right)\left(\underbrace{\frac{\partial}{\partial x_2}\frac{\partial}{\partial x_2}\overline{q'u'_2}}_{8}\right) + \underbrace{\rho \overline{q' E'_2 Q}}_{9} + \underbrace{\rho \overline{q'^2 E_2}}_{10} + \underbrace{\rho \overline{q'^2 E'_2}}_{11}. \quad (6.9)$$

Terms which now differ from a conventional passive scalar turbulent transport equation are the averaged terms resulting from the decomposition and averaging of the ionic drift term (terms 3–6) and the body force terms (terms 9–11); all of the other terms are identical as in the equation for the turbulent scalar flux of a passive scalar. More information on the meaning of these terms may be found in Kourmatzis & Shrimpton (2009).

We wish to study the budget of this main hydrodynamic turbulence production term, as discussed in §6.5.2, and therefore the transport equation for the flux term $\kappa \overline{q'E'_2}$, which is negligible in the domain bulk is not examined here:

$$\frac{\partial \rho\kappa \overline{q'E'_2}}{\partial t} + \frac{\partial \rho\kappa \overline{q'u'_2 E'_2}}{\partial x_2} + \frac{\partial \rho\kappa^2 \overline{q'E'_2 E'_2}}{\partial x_2} + \rho^2\kappa \frac{\overline{q'^2 u'_2}}{D_V} + \kappa^2\rho^2 \frac{\overline{q'^2 E'_2}}{D_V} + \overline{E'_2 u'_2}\frac{\partial \rho\kappa \overline{Q}}{\partial x_2}$$

$$+ \overline{E'_2 E'_2}\frac{\partial \rho\kappa^2 \overline{Q}}{\partial x_2} + \overline{q'u'_2}\frac{\rho^2\kappa \overline{Q}}{D_V} + \kappa^2\rho^2 \overline{E_2}\frac{\overline{q'^2}}{D_V} + 3\overline{q'E'_2}\frac{\kappa^2\rho^2 \overline{Q}}{D_V} + \frac{\partial \rho\kappa \overline{E_2}\,\overline{q'E'_2}}{\partial x_2}$$

$$= \frac{\partial}{\partial x_2}\frac{\kappa\mu}{Sc_Q}\frac{\partial}{\partial x_2}\overline{q'E'_2} + \frac{\rho}{D_V}\frac{\kappa\mu}{Sc_E}\frac{\partial \overline{q'^2/2}}{\partial x_2}. \quad (6.10)$$

Figure 13 plots terms 1–11 from (6.9) again as a function of y/d for case S2. Close to the wall the main source term is pressure scrambling (term 7) and is balanced by molecular diffusion (term 8) of the scalar flux and by the EHD body force term 9. Moving away from the wall the pressure scrambling stays as a source term along with term 5, the production of turbulent scalar flux acting on the mean electric field. Furthermore, the turbulent transport of space charge (term 2) also acts as a source and is counteracted by term 1. The other main sink term is the space charge variance EHD body force term 10 balanced by pressure scrambling (term 7) at the top wall. The pressure scrambling term in conventional turbulence acts to make the turbulent scalar flux more isotropic and here, it is observed that the dominant EHD body force term 10 acts as a significant sink throughout most of the domain showing here how EHD terms are hindering the action of pressure scrambling. The dominant EHD term 10 involves the turbulent scalar variance $\overline{q'^2}$ and is thus another budget that must be investigated, and also one of the turbulent transport equations that Hopfinger & Gosse derived as a product of their analysis. The scalar variance in RBC does not affect the turbulent scalar flux budget and therefore on a statistical level we see that there are differences between RBC and EHD regarding the transport of turbulent scalar fluctuations.

Attention is now drawn to term 9 of (6.9), a quantity which would have been neglected by Hopfinger & Gosse. This term is seen to act as the main sink term next to the bottom wall, as it is of greater magnitude than the molecular diffusion, making it effectively the only term that balances out the pressure scrambling close to the wall. As with the k_e distribution, fluctuations in the electric field in this instance are shown to have a very important role to play and therefore should be taken into consideration if models are to be proposed. Here, the electric field fluctuation present is analogous to the velocity fluctuation in the turbulent scalar flux term $\overline{q'u_2'}$ only now the vector component responsible for the turbulent convection of the space charge is E_2'. From a Reynold's stress modelling (RSM) point of view it may be said here that the only terms that need modelling from this transport equation are 7 and 2 as transport equations may be derived for all of the other relevant EHD second-order moments, namely the correlation between charge and electric field $\overline{q'E_2'}$ and the space charge variance $\overline{q'^2}$. Clearly, term $\overline{q'^2}$ is very significant throughout the bulk of the domain and therefore the transport equation for $\overline{q'^2}$ is stated and its budget discussed in the following section.

6.5.4. *Turbulent scalar variance budget*

The transport equation for the turbulent scalar variance $\overline{q'q'}$, which appeared in (6.6), when employing the same assumptions as for (6.8) is

$$\rho^2 \left[\frac{\partial \overline{(q'^2/2)}}{\partial t} + \kappa \left[\underbrace{\frac{2\rho \overline{Q}\,\overline{q'^2}}{D_V}}_{1} + \underbrace{\overline{q'E_2'}\frac{\partial \overline{Q}}{\partial x_2}}_{2} + \underbrace{\overline{E_2}\frac{\partial \overline{(q'^2/2)}}{\partial x_2}}_{3} + \underbrace{\frac{\partial}{\partial x_2}\overline{q'q'E_2'}}_{4} \right] \right]$$

$$+ \rho^2 \left[\underbrace{\overline{q'u_2'}\frac{\partial \overline{Q}}{\partial x_2}}_{5} + \underbrace{\frac{\partial}{\partial x_2}\overline{q'q'u_2'}}_{6} - \underbrace{D_Q\frac{\partial^2 \overline{(q'^2/2)}}{\partial x_2 \partial x_2}}_{7} + \underbrace{D_Q\overline{\left(\frac{\partial q'}{\partial x_2}\right)^2}}_{8} \right] = 0. \qquad (6.11)$$
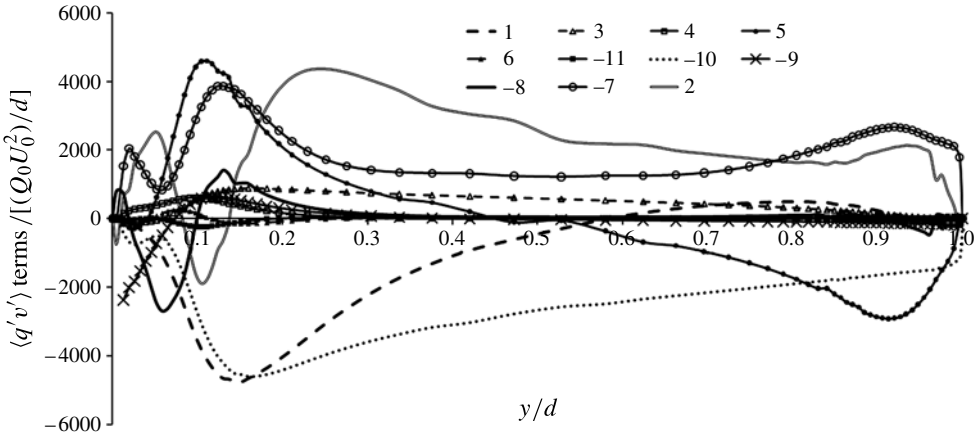
FIGURE 13. Budget of turbulent scalar flux $\overline{q'u_2'}$ for S2 case of table 1 as a function of y/d where v in the figure is equivalent to u_2.
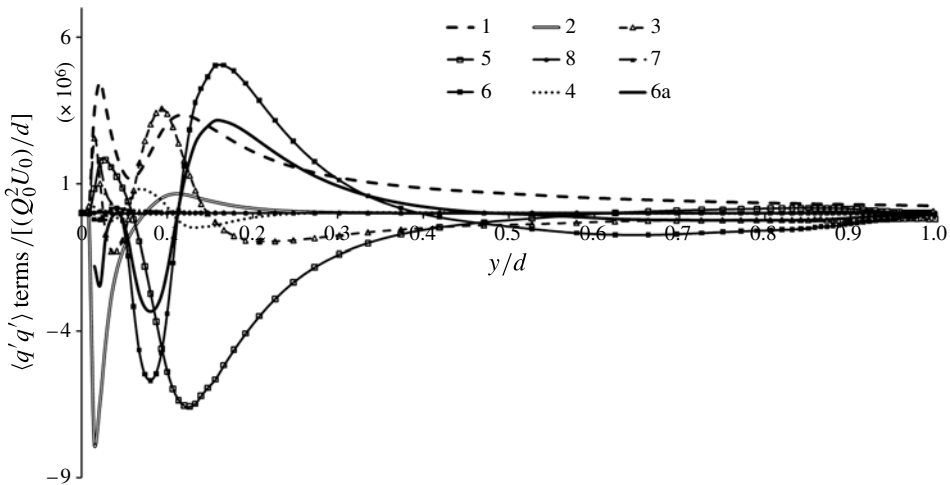

FIGURE 14. Budget of turbulent scalar variance $\overline{q'q'}$ for S2 case of table 1 as a function of y/d.

This equation was also presented by Hopfinger & Gosse (1971) but did not include terms 2 and 4. The budget for this equation is provided in figure 14 with the turbulent transport term calculated directly (term 6 in figure 14) while also using the method outlined in §6.5.2 (term 6a in figure 14). Terms that are different when compared to a passive scalar variance equation are those resulting from decomposition and averaging of the ionic drift component, seen here from terms 1–4.

As shown in figure 14, at the bottom wall the correlation of charge–electric field acting on mean charge gradient (term 2) acts as a sink and this is clearly a very significant term, and one neglected by Hopfinger & Gosse. It serves to balance terms 1, 3, and 5, which are the variance acting on the mean space charge, the variance gradient acting on the mean electric field and the turbulent scalar flux $\overline{q'u_2'}$ acting

on the mean charge gradient, the latter being effectively the production of the space charge variance by the turbulent scalar flux acting on the mean charge gradient.

Closer to the middle of the domain, the main two sources are terms 6 and 1 where term 6 is a turbulent transport of the variance, and the terms are counteracted by term 5 which appeared as a source close to the bottom wall. There is a discrepancy between the direct calculation of term 6, and calculation based on the sum of all of the other terms (term 6a). Averaging for longer did not result to a change in this observation; however it is clear that the two curves follow the same profile confirming that the physics is captured. The error is likely to be due to energy not being transferred from the small unresolved electrical length scales to the hydrodynamic scales, and is significant as it is a third-order correlation resulting in an error of greater magnitude. The maximum error calculated is approximately 36 % but the reader should note that the two curves are qualitatively identical.

At the top of the domain the scalar variance is quite low, further showing the nonlinearity of the space charge field and how any contributions to the scalar variance occur close to the bottom wall.

Molecular diffusion of the scalar variance is entirely negligible, which is to be expected given the very small ionic mobilities. Dissipation has some presence close to the bottom wall but is again generally negligible. The reader should note however that if gradients of these budgets were calculated based on sub-Kolmogorov electrical scales, their magnitude would be significantly larger, therefore contributing more to the energy budget.

7. Conclusions

The paper has presented qualitative and quantitative results analysing the structure of three-dimensional electroconvection in dielectric liquid insulators both deterministically and statistically. Two-dimensional results have been compared with the literature (Vazquez *et al.* 2006, 2008) and confirm simulations carried out by researchers in the field. Strong injection cases were run in two and three dimensions. The three-dimensional EHD simulations show a more chaotic nature with a distribution of length scales, which are observations that could not have been made from two-dimensional domains. Two-point correlations showed that the strong injection cases with $Re_E = 60$ and $Re_E = 120$ were closest to the RBC case in terms of spatial size variation. Spectral analysis revealed how turbulent kinetic and electrical energy is distributed amongst wavenumbers for the various cases run. Turbulent kinetic energy is created and dissipated over a wider range of wavenumbers when compared to electrical energy and the conversion of turbulent electrical energy to kinetic energy was further investigated by analysing spectra as a function of vertical position. Second-order moments of turbulent kinetic energy, turbulent electrical energy, turbulent scalar flux and turbulent scalar variance were analysed and it was found that the turbulent kinetic energy and turbulent scalar flux followed similar trends as with the RBC case though the distribution of k was not as spatially uniform for the EHD cases. The assumption by Hopfinger & Gosse (1971) stating that E_i' is negligible, was revisited, and it was determined that close to the walls the assumption is invalid, making the modelling of EHD turbulence much more complex for practical problems. The budgets of turbulent kinetic energy, turbulent scalar flux and turbulent scalar variance were analysed with respect to vertical position y/d and the results revealed dominant terms acting as sources and sinks. There is an inevitable inherent error with the higher-order moment and budget calculations due to the very large Schmidt number of the problem; however

this initial investigation has provided invaluable fundamental information regarding the physics of three-dimensional EHD turbulence, and the research has revealed practical information regarding what terms must be closed in EHD turbulence if modelling is to be undertaken using a Reynolds stress closure approach.

REFERENCES

ATTEN, P. 1996 Electrohydrodynamic instability and motion induced by injected space charge in insulating liquids. *IEEE Trans. Dielec. Elec. Insul.* **3**, 1–17.

ATTEN, P. 1998 Instability and convection induced by injected space charge. In *Electrohydrodynamics*, 1st edn (ed. A Castellanos). Springer.

BAILEY, A. G. 1986 The theory and practice of electrostatic spraying. *Atomiz. Spray Technol.* **2**, 95–134.

BALACHANDRAN, W., MACHOWSKI, W., HALIMIC, M., MORGAN, L., GRAY, C. & WILSON, C. 1999 Development of an electrostatic nozzle for gas turbine applications. In *Proceedings of ILASS, Toulouse, France*. ILASS.

BANKSTON, C. P., BACK, L. H., KWACK, E. Y. & KELLY, A. J. 1988 Experimental investigation of electrostatic dispersion and combustion of diesel fuel jets. *Trans. ASME: J. Engng Gas Turbines Power* **110**, 361–368.

BATCHELOR, G. K. 1959 Small-scale variation of convected quantities like temperature in turbulent fluid. *J. Fluid Mech.* **5**, 113–133.

CASTELLANOS, A. 1991 Coulomb-driven convection in electrohydrodynamics. *IEEE Trans. Elec. Insul.* **26**, 1201–1215.

CASTELLANOS, A. 1998 Basic concepts and equations in electrohydrodynamics. In *Electrohydrodynamics*, 1st edn (ed. A. Castellanos). Springer.

CASTRO, I. P. 1989 *An Introduction to the Digital Analysis of Stationary Signals*. IOP.

CHANDRA, L. & GROTZBACH, G. 2008 Analysis and modelling of the turbulent diffusion of turbulent heat fluxes in natural convection. *Intl J. Heat Fluid Flow* **29**, 743–751.

CHAVANNE, M. X., CHILLA, F., CHABAUD, B., CASTAING, B. & HEBRAL, B. 2001 Turbulent Rayleigh Benard convection in gaseous and liquid He. *Phys. Fluids* **13**, 1300–1320.

CHICON, R., CASTELLANOS, A. & MARTIN, E. 1997 Numerical modelling of Coulomb-driven convection in insulating liquids. *J. Fluid Mech.* **344**, 46–66.

CROWLEY, J. M. 1999 *Fundamentals of Applied Electrostatics*. Laplacian.

DAVIDSON, J. H. & MCKINNEY, P. J. 1989 Turbulent mixing in a barbed plate-to-plate electrostatic precipitator. *Atmos. Environ.* **23**, 2093–2107.

DAVIDSON, J. H. & MCKINNEY, P. J. 1991 EHD flow visualization in the wire-plate and barbed plate electrostatic precipitator. *IEEE Trans. Ind. Applics.* **27**, 154–160.

ECKHARDT, B., GROSSMAN, S. & LOHSE, D. 2007 Fluxes and energy dissipation in thermal convection and shear flows. *Europhys. Lett.* **78** (24001), 1–6.

GETLING, A. V. 1998 *Rayleigh Benard Convection, Structures and Dynamics*. World Scientific.

HONG, L., WANG, L.-Z. & WU, Z.-N. 2008 EHD turbulent flow and monte-carlo simulation for particle charging and tracing in a wire-plate electrostatic precipitator. *J. Electrostat.* **66**, 130–141.

HOPFINGER, E. J. & GOSSE, J. P. 1971 Charge transport by self-generated turbulence in insulating liquids submitted to unipolar injection. *Phys. Fluids* **14**, 1671–1682.

KELLY, A. J. 1984 The electrostatic atomization of hydrocarbons. *J. Inst. Energy* **57**, 312–320.

KELLY, A. J. 1990 Charge injection electrostatic atomizer modelling. *Aerosol Sci. Technol.* **12**, 526–537.

KERR, R. M. 2001 Energy budget in Rayleigh-Benard convection. *Phys. Rev. Lett.* **87** (244502), 1–4.

KIM, K. & TURNBULL, J. 1976 Generation of charged drops of insulating liquids by electrostatic spraying. *J. Appl. Phys.* **47**, 1964–1969.

KOURMATZIS, A. & SHRIMPTON, J. 2009 Electrohydrodynamics and charge injection atomizers: a review of the governing equations and turbulence. *Atomiz. Sprays* **19**, 1045–1063.

KOURMATZIS, A. & SHRIMPTON, J. S. 2012 Simulation of dielectric liquid electrohydrodynamic (EHD) convection with a conventional finite volume scheme, *Intl J. Numer. Meth. Fluids* (submitted).

LACROIX, J. C., ATTEN, P. & HOPFINGER, E. J. 1975 Electro-convection in a dielectric liquid layer subjected to unipolar injection. *J. Fluid Mech.* **69**, 539–564.

LEHR, W. & HILLER, W. 1993 Electrostatic atomization of liquid hydrocarbons. *J. Electrostat.* **30**, 433–440.

MELCHER, R. J. 1981 *Continuum Electromechanics*. MIT.

PEREZ, A. T., TRAORE, P. H., KOULOVA-NENOVA, D. & ROMAT, H. 2009 Numerical study of an electrohydrodynamic plume between a blade injector and a flat plate. *IEEE Trans. Dielec. Elec. Insul.* **16**, 448–455.

POPE, S. B. 2000 *Turbulent Flows*. Cambridge University Press.

RIGIT, A. R. H & SHRIMPTON, J. S. 2006 Spray characteristics of charge injection electrostatic atomizers with small-orifice diameters. *Atomiz. Sprays* **16**, 421–442.

SCHNEIDER, J. M. & WATSON, P. K. 1970 Electrohydrodynamic stability of space-charge-limited currents in dielectric liquids. Part I. Theoretical study. *Phys. Fluids* **13**, 1948–1954.

SHISHKINA, O. & WAGNER, C. 2006 Analysis of thermal dissipation rates in turbulent Rayleigh Benard convection. *J. Fluid Mech.* **546**, 51–60.

SHRIMPTON, J. & KOURMATZIS, A. 2010 Direct numerical simulation of forced flow dielectric EHD within charge injection atomizers. *IEEE Trans. Dielec. Elec. Insul.* **17**, 1838–1845.

SHRIMPTON, J. S. & YULE, A. J. 2003 Electrohydrodynamics of charge injection atomization: Regimes and fundamental limits. *Atomiz. Sprays* **12**, 173–190.

SOLDATI, A. & BANERJEE, S. 1998 Turbulence modification by large-scale organized electrohydrodynamic flows. *Phys. Fluids* **10**, 1742–1756.

TOBAZEON, R. 1984 Electrohydrodynamic instabilities and electroconvection in the transient and A.C. regime of unipolar injection in insulating liquids: A review. *J. Electrostat.* **15**, 359–384.

TRAORE, P. H., PEREZ, A. T., KOULOVA, D. & ROMAT, H. 2010 Numerical modelling of finite-amplitude electro-thermo-convection in a dielectric liquid layer subjected to both unipolar injection and temperature gradient. *J. Fluid Mech.* **658**, 279–293.

VAZQUEZ, P. A., GHEORGIOU, G. E. & CASTELLANOS, A. 2006 Characterization of injection instabilities in electrohydrodynamics by numerical modelling: comparison of particle in cell and flux corrected transport methods for electroconvection between two plates. *J. Phys.* D: *Appl. Phys.* **39**, 2754–2763.

VAZQUEZ, P. A., GHEORGIOU, G. E. & CASTELLANOS, A. 2008 Numerical analysis of the stability of the electrohydrodynamic (EHD) electroconvection between two plates. *J. Phys.* D: *Appl. Phys.* **41**, 10pp.

VAZQUEZ, P. A., PEREZ, A. T. & CASTELLANOS, A. 1996 Thermal and electrohydrodynamic plumes. a comparative study. *Phys. Fluids* **8**, 2091–2096.

VERSTEEG, H. K. & MALALASEKERA, W. 1995 *An Introduction to Computational Fluid Dynamics*. Longman.

VERZICCO, R. & SREENIVASAN, K. R. 2008 A comparison of turbulent thermal convection between conditions of constant temperature and constant heat flux. *J. Fluid Mech.* **595**, 203–219.

WORNER, M. & GROTZBACH, G. 1998 Pressure transport in direct numerical simulations of turbulent natural convection in horizontal fluid layers. *Intl J. Heat Fluid Flow* **19**, 150–158.

WU, X.-Z., KADANOFF, L., LIBCHABER, A. & SANO, M. 1990 Frequency power spectrum of temperature fluctuations in free convection. *Phys. Rev. Lett.* **64**, 2140–2143.

XI, H.-W. & GUNTON, J. D. 1993 Spiral-pattern formation in Rayleigh-Benard convection. *Phys. Rev.* **47**, R2987–R2990.

YAMAMOTO, T., MORITA, Y., FUJISHUMA, H. & OKUBO, M. 2006 Three-dimensional EHD simulation for point corona electrostatic precipitator based on laminar and turbulent models. *J. Electrostat.* **64**, 628–633.

YE, Q., DOMNICK, A. S. & PULLI, K. 2005 Numerical simulation of electrostatic spray-painting processes in the automotive industry. *High Performance Comput. Sci. Engng* **4**, 261–275.

YEUNG, P. K., XU, S. & SREENIVASAN, K. R. 2002 Schmidt number effects on turbulent transport with uniform mean scalar gradient. *Phys. Fluids* **14**, 4178–4191.